

Master's Thesis

Ultrabroadband Enhancement Cavities for Nonlinear Optics

Christina Hofer



Technical University of Munich
Max Planck Institute of Quantum Optics, Garching

Munich, October 2016

Masterarbeit

Ultrabreitbandige
Überhöhungsresonatoren
für nichtlineare Optik

Christina Hofer

Technische Universität München
Max-Planck-Institut für Quantenoptik, Garching

Erstgutachter: Prof. Dr. Reinhard Kienberger
TU München, Institut für Laser - und Röntgenphysik
Betreuer: Dr. Ioachim Pupeza
Max-Planck-Institut für Quantenoptik, Garching

München, Oktober 2016

Abstract

The main goal of this thesis was the expansion of the bandwidth of an enhancement cavity above the state-of-the-art value of 100 nm. Firstly, this was done by building a cavity that supports sub-20-fs input pulses and finding a reliable characterization scheme for the intracavity pulses. Secondly, a proof of principle experiment on intracavity spectral broadening with narrow-band input pulses in a 100- μm -thick glass substrate was done, with the resulting spectral bandwidths being as broad as in the first experiment. This initiated a theoretical investigation of the applicability of such a nonlinear enhancement cavity for spectroscopy. To that end, the path length enhancements of linear and a nonlinear cavities with the same bandwidths and average power enhancements were compared.

Before the setup of a cavity that supports 20-fs pulses, a mirror combination, suitable for this cavity bandwidth, had to be found. This needed many different mirror designs and coating runs, as such broadband mirror coatings with flat phases are at the edge of what is possible with state-of-the-art coating techniques. The suitability of the mirrors for the use in the cavity was checked with a multi-pass-setup and spatial-spectral-interferometry (SSI) measurements. For the characterization of the intracavity pulse, two independent methods were developed. Method one measures the phase of the input pulse with frequency-resolved optical gating (FROG) and the phase of the cavity with SSI. Together with an independently measured intracavity spectrum, the pulse can be calculated from the measured quantities using a Fourier transform. The second method directly measures the intracavity pulse with FROG, using a beam produced by a clipping mirror in the cavity beam path.

The influence of the intracavity spectral broadening on the path length enhancement of the cavity was calculated with a simple 1D model of the nonlinear cavity including a linear absorption line. The first order propagation equation was used for the

simulation of the nonlinearity and the Lorentz oscillator model for the calculation of the linear absorption line. Both spatial effects and dispersion were neglected for this investigation. The absorption was calculated after the cavity buildup had reached a steady state.

With the above described methods for mirror and pulse characterization, an unprecedented intracavity pulse duration of sub-20 fs was demonstrated. The intracavity power was around 1 kW, with an average power enhancement of ≈ 70 and a finesse of ≈ 340 . For a laser pulse train with a central wavelength of 1050 nm, a pulse duration of 20 fs corresponds to 5.4 oscillations of the electric field. This brings us to the few-cycle-regime. With a suitable gating mechanism, the intracavity generation of isolated attosecond pulses via high harmonic generation would now be possible. The spectra that we measured in the intracavity spectral broadening experiment also had bandwidths that would support 20-fs pulses. The simulations of the path length enhancement of the nonlinear cavity show, that it strongly depends on the average power enhancement and the strength of the nonlinearity, which was varied by the thickness of the glass substrate for spectral broadening. For average power enhancements of around 60 and plate thicknesses below $100 \mu\text{m}$, the simulated path length enhancement surpassed the one of a linear enhancement cavity with the same average power enhancement. Further simulations of the interaction of the nonlinearity and the linear absorption still need to be done. Nevertheless, so far the nonlinear cavity seems to be suitable for spectroscopy.

Kurzzusammenfassung

Das Ziel dieser Arbeit war es, die bisher gezeigte Bandbreite eines Überhöhungsresonators von 100 nm weiter zu erhöhen. Dafür wurde zunächst ein Resonator gebaut, der die Eingangspulse, welche eine Pulsdauer von unter 20 fs haben, unterstützt. Weiters wurde eine Charakterisierungsmethode für die Pulse im Resonator entwickelt. Als zweites wurde ein Experiment zur spektralen Verbreiterung eines Laserpulses in einem 100 μm dicken Glasplättchen im Fokus eines Resonators durchgeführt. Die Bandbreiten der dabei gemessenen Spektren entsprachen denen des ersten Experiments. Um die Anwendbarkeit eines solchen nichtlinearen Resonators für Spektroskopie zu untersuchen, wurde dessen Weglängenüberhöhung mittels Simulationen mit der eines linearen Resonators mit der gleichen Bandbreite und mittleren Leistungsüberhöhung verglichen.

Bevor ein Resonator, welcher 20 fs Pulse unterstützt, aufgebaut werden konnte, musste eine dafür geeignete Spiegelkombination gefunden werden. Da es am Rande des derzeit technisch Möglichen ist, Spiegel herzustellen, welche für die zu erreichende Bandbreite eine flache Phase haben, mussten dafür zunächst viele Spiegeldesigns - und coatings gemacht werden. Wir überprüften mittels eines Multipass-Aufbaus und räumlich-spektraler Interferometrie (SSI), ob die hergestellten Spiegel für die Verwendung im Resonator geeignet sind. Zur Charakterisierung der Pulse wurden zwei von einander unabhängige Methoden entwickelt. Bei der ersten wird die Phase des Eingangspulses mittels frequenz aufgelöstem optischem Gating (FROG) und die Phase des Resonators mittels räumlich-spektraler Interferometrie gemessen. Zusammen mit dem unabhängig davon gemessenen Spektrum des Pulses im Resonator, kann dieser mittels einer Fouriertransformation errechnet werden. Die zweite Methode misst mittels FROG den zirkulierenden Puls direkt in einem geklippten Strahl, der durch das minimale Hineinführen eines Spiegels in den Strahlweg erzeugt wird.

Die Wechselwirkung der Nichtlinearität und der linearen Absorption im Resonator wurde mittels der Propagationsgleichung erster Ordnung für die Nichtlinearität und dem Lorentz Modell für die Absorption simuliert. Dabei wurden räumliche Effekte und Dispersion vernachlässigt. Die Absorption wurde zudem erst dann betrachtet, nachdem sich im Resonator ein Gleichgewichtszustand nach dem Aufbau des Pulses eingestellt hatte.

Mit den oben beschriebenen Methoden zur Spiegel - und Pulscharakterisierung, wurden Pulsdauern unter 20 fs im Resonator gemessen, was so bisher noch nie gezeigt wurde. Die Leistung im Resonator betrug bei einer Überhöhung von ≈ 70 und einer Finesse von ≈ 340 ungefähr 1 kW. Für die Zentralwellenlänge des Pulses von 1050 nm, entspricht diese Pulsdauer 5.4 Schwingungszyklen des elektrischen Feldes. In diesem Pulsdauer-Bereich wäre es möglich, mittels der Generation von hohen Harmonischen und einer passenden Gating-Methode, isolierte Attosekunden-Pulse in dem Resonator zu erzeugen.

Auch jene Spektren, welche wir in einem Glasplättchen im Resonator verbreiterten, erreichten Bandbreiten, die 20 fs Pulse unterstützen würden. Die Simulationen der Weglängenüberhöhung in einem nichtlinearen Resonator ergaben, dass diese Überhöhung sehr von der Stärke der Nichtlinearität, welche durch die Dicke des Glasplättchens variiert wurde, und der mittleren Überhöhung des Pulses abhängt. Für Überhöhungen im Bereich von 60 und Plättchendicken unter $100 \mu\text{m}$ konnten Wechselwirkungslängen simuliert werden, die über der linearen Überhöhung, welche durch die Finesse des Resonators gegeben ist, liegen. Weitere und genauere Simulationen dieser Wechselwirkung sind noch notwendig, die bisherigen Ergebnisse zeigen jedoch, dass auch ein nichtlinearer Resonator für Spektroskopie geeignet sein sollte.

Contents

1	Introduction	1
2	Theoretical Background	5
2.1	Ultra-short laser pulses	5
2.2	Enhancement cavities	8
2.3	Phase-sensitive laser pulse measurement techniques	14
2.3.1	Frequency Resolved Optical Gating (FROG)	15
2.3.2	Spatial Spectral Interferometry (SSI)	21
3	Experiments	23
3.1	Ultrabroadband linear enhancement cavities	23
3.1.1	Setup	24
3.1.2	Characterization of the cavity mirrors	26
3.1.3	Results: Cavity Bandwidth	28
3.1.4	Characterization of the intracavity pulse	30
3.1.5	Results: Intracavity pulse duration	33
3.2	Intracavity spectral broadening and pulse compression	38
3.2.1	Setup	38
3.2.2	Results	39
4	Simulation of intracavity spectral broadening	47
4.1	Propagation of laser pulses through a Kerr medium	48
4.2	Buildup in a nonlinear enhancement cavity	49
4.3	Kerr nonlinearity vs. linear absorption in a cavity	50
5	Conclusion and outlook	59
6	Bibliography	61

Chapter 1

Introduction

Passive optical resonators, also called enhancement cavities (ECs) have been used for the resonant enhancement of continuous wave or pulsed lasers for many years [1]. On the one hand, they can enhance the average and peak power of a laser by several orders of magnitude. This is especially useful for conversion processes with very low efficiency like high harmonic generation (HHG) or Thomson scattering, for which it is beneficial to reuse the unconverted photons [2, 3]. On the other hand, an EC drastically increases the sensitivity of light to dispersion or absorption inside of it. This has advantages and disadvantages. It is beneficial in the case of intracavity spectroscopy, because the effective interaction length of a laser pulse with the probed medium is increased proportionally to the cavity finesse, which can be several orders of magnitude [4]. Methods which use this effect are cavity enhanced absorption [5] and Raman spectroscopy [6, 7]. Furthermore, direct frequency comb spectroscopy, in the infrared (IR) and ultraviolet (UV) spectral region, has already been implemented [8–11].

However, the sensitivity enhancement becomes crucial in the case of intracavity dispersion. Spectral phase distortions on the order of a few mrad can already distort the intracavity pulse significantly and cause a mismatch of the modes of the input pulse train and the cavity resonances, which leads to a reduction of the enhancement [1]. The production of cavity mirrors with a flat phase over a broad spectral bandwidth is technically challenging, because variations of the layer thicknesses on the order of several nanometers can already cause phase distortions. State-of-the-art ECs support bandwidths of about 100 nm and below [12].

One goal of our group, was to clearly surpass these bandwidths, in order to access

the few-cycle regime for near-infrared (NIR) pulses, where the generation of isolated attosecond pulses becomes feasible with suitable gating techniques [13, 14]. For this purpose, many mirror designs and coating runs, were made. However, produced mirror phases differ significantly from the target design for most broadband coating runs. Therefore, the characterization of the cavity mirrors plays an important role. This can be done with a multipass setup for sensitivity enhancement, and the spatial spectral interferometry (SSI) technique [15], which can measure the relative mirror phase, with respect to a reference beam. After suitable cavity mirrors had been selected, one main goal of this thesis was the reliable characterization of the intracavity pulse. This is not trivial, as the cavity properties should not be affected by the measurement. Additionally, the pulse should be modulated as little as possible when propagating from the cavity to the measurement apparatus, which, for example, can be frequency resolved optical gating (FROG).

As described above, building an EC that supports ultrashort laser pulses is challenging with state-of-the-art mirror coating techniques. Furthermore, pulse shortening techniques, like spectral broadening in a fibre and subsequent compression of the pulses with chirped mirrors (CMs) are often troublesome to align and limited in pulse power. Therefore we pursued the idea to transfer this spectral broadening process inside the cavity. As shown in a proof-of-principle experiment, this is feasible with self-phase-modulation (SPM) in a fused-silica (FS) substrate that is placed in the cavity focus. However, the intracavity pulse compression is challenging, as the pulse duration influences the nonlinearity. Therefore, simulations of the needed shape of the phase of the cavity mirrors for self compression are necessary. Nevertheless, these first intracavity spectral broadening experiments gave the incentive for the investigation of the influence of spectral broadening on the sensitivity enhancement of the cavity. This should answer the question, whether the spectrally broadened pulses, which would not even have to be compressed, could still be used for spectroscopy, which is one of the key applications of an EC. This way, we would obtain an easy-to-generate, very broad spectrum inside an EC, with applications in, for example, stimulated Raman or absorption spectroscopy [16, 17].

This thesis is structured as follows: In the next chapter, a theoretical overview of the most important aspects needed for understanding the experiments and simulations is given. These are frequency combs and ECs on the one hand, and pulse or phase

characterization techniques like FROG and SSI on the other hand. The third chapter covers the description of the experiments that were carried out in the scope of this thesis. Firstly, this is the reliable characterization of the pulses inside an EC that supports 20 fs pulses. Secondly, the proof of principle experiment on intracavity spectral broadening is described. This initiated the simulations in the last chapter, which investigate the influence of the nonlinear broadening inside the cavity on its sensitivity enhancement in absorption spectroscopy.

Chapter 2

Theoretical Background

This chapter is a short summary of the most important basic facts needed to understand the experiments and simulations presented in this thesis. Firstly, ultra-short laser pulses and frequency combs will be introduced. The second part covers the basic equations for describing ECs and their transverse modes. In the last section, the spectral phase measurement techniques FROG and SSI are explained.

2.1 Ultra-short laser pulses

Complex representation of a laser pulse

In the following, we will proceed in close analogy to [18]. Laser pulses can be described as complex numbers either in the time or the frequency domain. Neglecting spatial and polarization dependencies, the real valued electric field only depends on time ($E(t)$) and the field in the frequency domain can be calculated as the Fourier transform (FT):

$$\tilde{E}(\omega) = \mathcal{F}_t(E(t)) = \left| \tilde{E}(\omega) \right| e^{i\varphi(\omega)} \quad (2.1)$$

with the spectral amplitude $|E(\omega)|$ and phase $\varphi(\omega)$. As we only want to use positive frequencies (indicated in the following by +), a complex field can also be defined in the time domain. The two domains are related as follows:

$$\begin{aligned} E^+(t) &= \frac{1}{2\pi} \int_{-\infty}^{\infty} \tilde{E}^+(\omega) e^{i\omega t} d\omega \\ \tilde{E}^+(\omega) &= \int_{-\infty}^{\infty} E^+(t) e^{-i\omega t} dt \end{aligned} \quad (2.2)$$

The complex field in the time domain can then be represented by an amplitude $\mathcal{E}(t)$ and a phase $\Gamma(t)$:

$$E^+(t) = \frac{1}{2}\mathcal{E}(t)e^{i\Gamma(t)} = \frac{1}{2}\mathcal{E}(t)e^{i(\varphi_0+\varphi(t))}e^{i\omega_c t} = \frac{1}{2}\tilde{\mathcal{E}}(t)e^{i\omega_c t} \quad (2.3)$$

where $\tilde{\mathcal{E}}(t)$ is the complex field envelope. The constant carrier-envelope (CE) offset phase slip φ_0 will be explained below. The so-called carrier frequency is written as ω_c and defined to minimize the time-dependent phase $\varphi(t)$. This definition is only useful for pulses with a bandwidth $\Delta\omega$ fulfilling $\frac{\Delta\omega}{\omega_c} \ll 1$, which means that the amplitude and phase vary slowly over one optical cycle. In general, ω_c corresponds to the intensity-weighted average frequency, which is the same in the time and the frequency domain.

The duration of a laser pulse can be defined in many ways, due to the many different possible pulse shapes, which also cannot be measured easily. One common way, is to use the Full Width at Half Maximum (FWHM) of $|\tilde{\mathcal{E}}(t)|^2$ and $|\tilde{\mathcal{E}}(\omega)|^2$, for the definition of the temporal width τ_p and the spectral width $\Delta\omega_p$, respectively. As the fields in the time and the frequency domain are related via a FT, $\Delta\omega_p$ and τ_p cannot be varied independently. Their product has a fixed lower limit c_B , which is called the time-bandwidth-product:

$$\Delta\omega_p\tau_p = 2\pi\Delta\nu_p\tau_p \geq 2\pi c_B \quad (2.4)$$

The value of c_B is pulse-shape dependent (e.g., $c_B = 0.441$ for a Gaussian pulse shape [18]). Pulses which fulfill equality in equation 2.4 are called bandwidth-limited or FT-limited pulses. They have the shortest possible pulse duration for a given bandwidth.

The problem of pulse shape determination will be addressed in chapter 2.3.1.

Frequency combs

The information in this section is mainly from [19]. Let us consider two laser pulses with the carrier frequency ω_c , that are propagating in a pulse train and are separated by a fixed time T . These pulses are not identical, because the envelope travels with

the group velocity of the medium it is propagating through, unlike the electric field which travels with the phase velocity. Therefore, the field is shifted by $\Delta\varphi = \varphi_0$ under the envelope from pulse to pulse. This is called the CE phase slip. The pulse envelope $A_{\text{env}}(t)$ can be assumed to be periodic in time, because of the modelocking process that generated the pulse train. In this process, the higher order phase terms that cause dispersion, are compensated by the mode-locking nonlinearity (e.g. self-phase-modulation). As a consequence, the pulses can propagate with no change of shape [20]. The electric field of this pulse train is then given by:

$$E(t) = \text{Re} [A_{\text{env}}(t)e^{-i\omega_c t}] = \text{Re} \left[\sum_n E_n(\omega) e^{-i(\omega_c + n\omega_r)t} \right] \quad (2.5)$$

This means, that the spectrum is a comb of longitudinal laser modes $E_n(\omega)$, where the n 'th comb line has the frequency $\omega_n = n\omega_r + \omega_0$. The repetition rate of the laser pulses is denoted as ω_r and ω_0 is the CE offset frequency, which is related to the phase slip φ_0 via $\omega_0 := \omega_{\text{ceo}} = -\frac{\varphi_0}{2\pi}\omega_{\text{rep}}$ [19, 21]. For femtosecond pulses, n is on the order of $10^5 - 10^6$. Both, ω_r and ω_0 are radiofrequencies. ω_r can be readily measured with a photodiode, whereas it is more difficult to measure ω_0 . For example, this can be done with an f-2f-interferometer [22, 23].

Spectral phase of a laser pulse

The phase of the laser pulse in the frequency domain, $\varphi(\omega)$ can be Taylor-expanded around the carrier frequency ω_c , according to [18]:

$$\varphi(\omega) \approx \varphi_0 + \varphi_1(\omega - \omega_c) + \frac{\varphi_2}{2}(\omega - \omega_c)^2 + \dots \quad (2.6)$$

The constant term φ_0 is again the CE offset phase slip, often also written as $\Delta\varphi$. The linear term φ_1 corresponds to a group delay (GD). Higher order terms, starting from the second order group delay dispersion (GDD), cause a laser pulse to change its shape and will play a major role when discussing ECs and the measurement of ultrashort laser pulses.

2.2 Enhancement cavities

The schematic of a possible mirror configuration for a passive optical resonator or EC is depicted in figure 2.1. It is a ring resonator, consisting of four mirrors, where one is called the input coupler (IC), which has a transmission on the order of 1%, and all other mirrors are as highly reflective (HR) as possible [24].

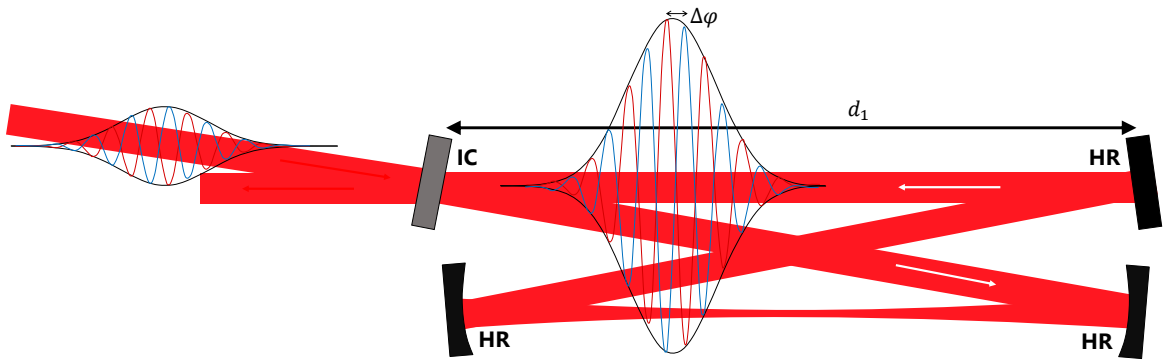


Figure 2.1: Typical setup of an Enhancement Cavity (EC). IC: Input Coupler. HR: Highly reflective mirror. For maximum enhancement, the cavity roundtrip-time has to match the input pulse repetition rate. In addition, the CE phase slip $\Delta\phi$ has to be the same for both frequency combs.

For the efficient enhancement of a pulse in an EC, the following requirements have to be met:

Considered in the time domain, the repetition rate of the input laser pulse train has to be set to match the cavity length L . In this way, after each roundtrip, a new pulse is overlapped with the intracavity pulse. Furthermore, the laser has a CE offset phase slip $\Delta\phi$ as described in section 2.1. For a certain input spectrum, the cavity has an optimal offset frequency (OOF). The best possible enhancement can be reached, if the offset frequency of the input pulse train is set to this value [25]. As a consequence, not only do the pulses' envelopes overlap perfectly at the IC, but the oscillating fields do as well [1].

In the frequency domain, the enhancement cavity has intrinsic resonance modes, just as the input frequency comb. The matching of these two combs for maximum enhancement will be explained using the sketch in figure 2.2 [26].

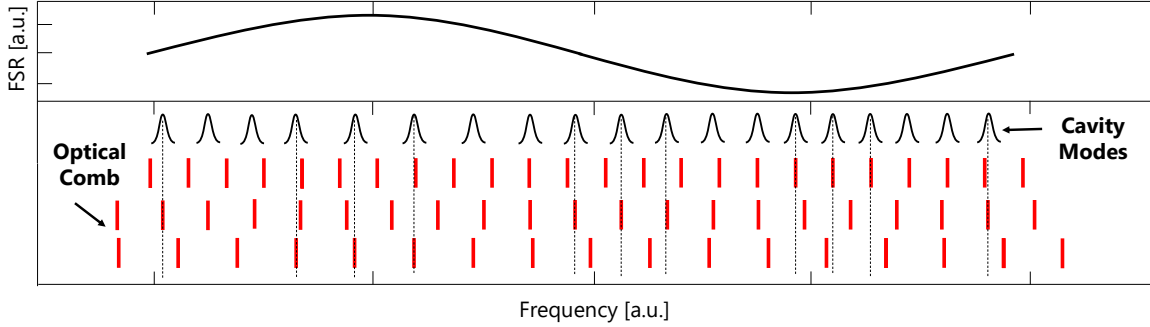


Figure 2.2: Sketch of the matching of the input pulse train to the cavity resonances. Upper part: Wavelength dependent Free Spectral Range (FSR). Lower part: Typical spacing of resonances in a dispersive cavity (black). Three possible laser combs, that fit to the cavity modes in different spectral ranges are shown in red. A perfect overlap of all laser and cavity modes is not possible due to the non-equidistant spacing of the cavity modes.

As described above, the laser modes are equidistantly spaced by the repetition rate ω_r and have an offset ω_0 from the zero frequency. From the consideration of the cavity in the steady state it will be clear, that this is not necessarily the case for the cavity resonances. In the steady state, the following equation holds for the complex envelope of the circulating electric field E_{circ} [27]:

$$E_{\text{circ}}(\omega) = \sqrt{T_{\text{ic}}(\omega)}E_{\text{in}}(\omega) + \sqrt{R_{\text{ic}}(\omega)}\sqrt{A(\omega)}e^{i\phi(\omega)}E_{\text{circ}}(\omega), \quad (2.7)$$

where E_{in} is the complex envelope of the the input field, T_{ic} and R_{ic} are the power transmission and reflectivity of the input coupler and A is the overall cavity roundtrip attenuation, which accounts for additional losses and mirror reflectivities < 1 . The total phase of the cavity is denoted as ϕ . The wavelength-dependent power enhancement U is then given by [27]:

$$U = \frac{|E_{\text{circ}}|^2}{|E_{\text{in}}|^2} = \frac{P_{\text{circ}}}{P_{\text{in}}} = \left| \frac{\sqrt{T_{\text{ic}}(\omega)}}{1 - \sqrt{R_{\text{ic}}(\omega)}\sqrt{A(\omega)}e^{i\phi(\omega)}} \right|^2 \quad (2.8)$$

with the input power P_{in} and the circulating intracavity power P_{circ} . The peaks in enhancement as a function of frequency would be equidistantly spaced for a constant cavity phase $\phi(\omega)$, mirror reflectivities and cavity losses. However, this is difficult to

reach, especially for broadband cavities. The cavity phase $\phi(\omega)$ consists of three parts:

1. The constant roundtrip CE phase slip $\Delta\varphi$, caused by the Gouy-phase from focusing a Gaussian beam (see transverse cavity modes, further down) and phase shifts from reflection and dispersion.
2. A linear phase shift (GD) caused by the cavity roundtrip time.
3. Higher-order terms, caused by chromatic dispersion due to the mirror coatings and intracavity media.

The constant and linear phases can be matched with ω_0 and ω_r of the laser. However, higher order terms, namely the dispersion, cause a variation of the free spectral range (FSR) over the spectrum of the incoming laser pulse, as depicted exemplary in the upper part of figure 2.2. Therefore the equidistant laser comb can never be perfectly matched to the passive cavity. This way, the cavity can act as a spectral filter [26]. Nevertheless, an optimum repetition rate and offset frequency can be found to reach the best possible overlap [25,26]. The width of the cavity modes is given by the finesse \mathcal{F} , which is a measure for the number of roundtrips a photon makes before it leaves the cavity. It is determined by the IC reflectivity and the cavity attenuation [27]:

$$\mathcal{F} = \frac{2\pi}{1 - R_{ic}(\omega)A(\omega)} \quad (2.9)$$

The lower the finesse, the broader the cavity resonances are. Therefore it is easier to match a laser comb to the cavity in the low-finesse case. A measure for acceptable phase variations is a corridor given by the phase distortions that cause the enhancement to drop to half the maximum value [28]. This is given by:

$$\Delta\phi_{\max} \approx \frac{\pi}{\mathcal{F}} \quad (2.10)$$

Therefore a trade-off between finesse and cavity bandwidth has to be found. However, the enhanced sensitivity of the cavity to (phase) distortions can also be useful, for example for spectroscopy or precise measurements of mirror phases.

In addition to the so-far considered longitudinal (spectral) cavity modes, a stable cavity also has intrinsic transverse spatial modes, that are given as the solutions of

the paraxial wave equation [24]. These are the so-called Gauss-Hermite modes, which are given by the following equation:

$$u(x, y, z) = \frac{w_0}{w(z)} H_n\left(\sqrt{2}\frac{x}{w}\right) H_m\left(\sqrt{2}\frac{y}{w}\right) \cdot \exp\left(-i(kz - \phi_g(m, n; z)) - i\frac{k}{q}(x^2 + y^2)\right), \quad (2.11)$$

where m and n are the indices of different transverse modes and indicate the number of minima in the field distribution. H_n and H_m are the Hermite Polynomials of order n and m [18]. The Gouy-phase ϕ_g , is given by:

$$\phi_g(m, n; z) = (n + m + 1) \arctan\left(\frac{z}{z_R}\right) \quad (2.12)$$

with the Rayleigh-length z_R [29]. In general, this phase differs for different transverse modes. As it has to be compensated for by the CE offset frequency of the input pulse train, the cavity acts as a spatial filter [12], which can be adjusted by changing the cavity length. In the following, the H_0 mode will be chosen to be the resonant spatial mode. The beam waist is denoted as w_0 and $w(z)$ is the beam radius. The complex beam parameter q , describing the geometric evolution of the beam, depends on the radius of curvature R and the beam radius w [24]:

$$\frac{1}{q(z)} = \frac{1}{R(z)} - i\frac{\lambda}{n_R\pi w(z)^2}, \quad (2.13)$$

where n_R is the refractive index of the material that the beam is propagating through. In a stable resonator, q has to reproduce itself after one cavity roundtrip. In a ring resonator like in figure 2.1, this leads to the following stability criterium for the distance d between the curved mirrors [24]:

$$R_m \leq d \leq \frac{R_m(d_1 + 2d_2)}{d_1 + 2d_2 - R_m}, \quad (2.14)$$

where R_m is the radius of curvature of the cavity mirrors, d_1 the distance between the plane mirrors (see figure 2.1) and d_2 separates a plane and a curved mirror (assuming a symmetric assembly). At the edges of this stability range, the mode size on the curved mirrors diverges, which is used for example in [30] to avoid mirror damages.

For the characterization of the intracavity pulses in our experiments, we used a beam

from a D-shaped clipping mirror in the cavity beam path. Therefore the spatial wavelength dependence of the intracavity beam is crucial. This can be derived from the stability criterion, that the radius of curvature of the cavity beam has to match the mirror radius of curvature R_m for all wavelengths at the position of the curved mirrors. The radius of curvature of the beam at the mirror position z_m is given by [24]:

$$R(z_{\text{mirror}}) = R_m = z_m \left(1 + \left(\frac{z_R}{z_m} \right)^2 \right) \quad (2.15)$$

Therefore the Rayleigh-length z_R also has to be wavelength-independent. The value of the Rayleigh-length can be calculated from the known beam radius on one cavity mirror w_m and the beam waist w_{focus} in the focus [24]:

$$z_R = \frac{z_{\text{mirror}}}{\sqrt{(w_{\text{focus}}/w_{\text{mirror}})^2 - 1}} \quad (2.16)$$

The wavelength dependent beam waist is given by $w_{\text{focus}}(\lambda) = \sqrt{\frac{z_R \lambda}{\pi}}$. As a consequence, the wavelength dependent beam radius of a Gaussian beam is then given as follows [24]:

$$w(\lambda) = w_0(\lambda) \sqrt{1 + \left(\frac{z}{z_R} \right)^2} \quad (2.17)$$

As $\frac{w}{w_0}$ is not wavelength dependent, the relative percentage of each wavelength is constant, but the overall beam size increases with the distance from the beam waist.

Modematching

For optimum enhancement, the q-parameters of the input pulse and the cavity have to match. In an adiabatic scan of the cavity length, where a cavity-buildup is possible for each length, the matching of the transverse spatial field of the input beam to the different transverse modes of the cavity can be seen. This is schematically depicted in figure 2.3 [29].

It shows the intracavity power as a function of the cavity length. The numbers stand for the sum of the mode indices of the Gaussian beam, $m + n$. In our experiment, we want to maximize the overlap of the spatial field of the input pulse with the H_0 mode of

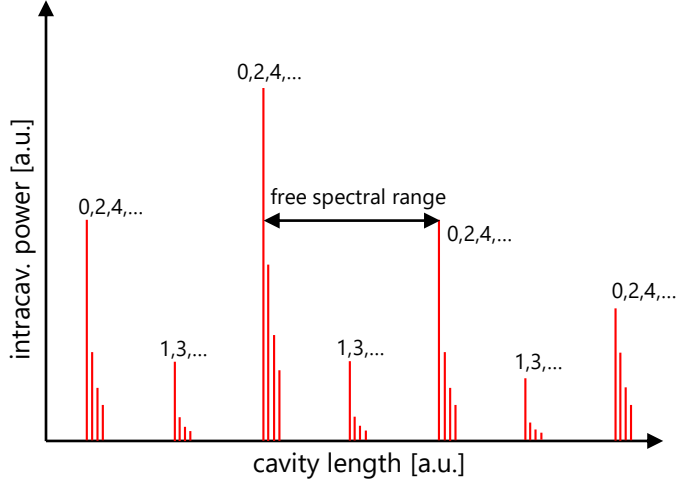


Figure 2.3: Schematic of the scan of the cavity length in the special case of nearly degenerate even and uneven modes. The numbers stand for the sum of the mode indices m and n of the Gaussian beam. The main resonances (H_0) are separated by the free spectral range, which corresponds to cavity length scan of one wavelength.

the cavity. This can be done by matching the Gaussian beam parameters of the input pulse to the cavity parameters with two lenses [24]. A possible configuration is shown in figure 2.4. To this end, first the beam radii of the input and intracavity beam at the IC (2.07 mm and 1.47 mm respectively) have to be measured. As the input beam is almost perfectly collimated, a flat phase front with a radius of curvature of $\approx \infty$ can be assumed. The radius of curvature of the intracavity beam can be calculated from the cavity geometry, when the beam radius is known at two positions. With these parameters, a set of lenses (in our exemplary case with the focal lengths of -50 mm and 75 mm) can be picked, which match the q-parameters of the two beams, when placed at a distance of about 25 mm.

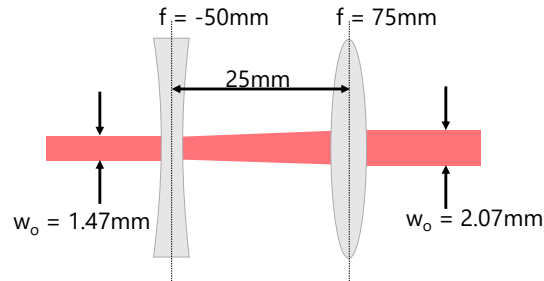


Figure 2.4: Setup for modematching of the input pulse train to the cavity. The beam radius at the cavity input coupler mirror is measured to be 2.07 mm, the one of the laser beam to be 1.47 mm. Two lenses with focal lengths -50 mm and 75 mm have to be placed in the beam path at a distance of 25 mm for matching the q-parameters of the input and intracavity beam.

2.3 Phase-sensitive laser pulse measurement techniques

For the complete characterization of a laser pulse, it is necessary to measure its time- or frequency-dependent intensity and phase. An autocorrelation (AC) measurement [18] can give the approximate time dependent pulse shape and the spectral shape can be measured easily by means of a spectrometer. Measuring the exact time-dependent intensity and phase, however, is a little bit more challenging. In 1993, Kane and Trebino demonstrated for the first time that this can be done with a technique called FROG, which is in principle a frequency-resolved AC measurement. All important facts concerning FROG can be found in [31] or [32]. Any nonlinear effect that can be used for AC measurements, can also be used for FROG. The pulse characterization in this thesis was done with a second harmonic generation (SHG) FROG [33,34]. Compared to direct field measurement techniques like attosecond streaking [35] or electro-optic sampling [36], this technique does not unambiguously determine the electric field of a laser pulse, but needs a sophisticated retrieval algorithm that computes the complex envelope and phase of the pulse.

When working with an EC, the phase of the cavity mirrors is crucial for the supported

spectral bandwidth. This phase can be measured with SSI [15]. In [37] and [21], it was used for measuring the complete phase of an EC. In contrast to FROG, SSI can only determine a phase difference between two pulses, but not the complete pulse information, consisting of the absolute phase and complex envelope.

The first section of this chapter gives an overview of the most important aspects concerning SHG FROG measurements. The second section is a short summary of the basic principles of SSI.

2.3.1 Frequency Resolved Optical Gating (FROG)

In a FROG measurement, two replica of a laser pulse are overlapped, with varying time delay, in a nonlinear crystal. The spectrum of the signal produced by the overlap, which is an autocorrelation signal, is measured as a function of the delay between the beams, leading to maximum signal at zero delay. In principle, all the nonlinear effects known from autocorrelation measurements can be used for FROG. Among these, SHG is the most efficient one, because it is a second order process. Therefore it is especially useful for characterizing weak pulses (on the order of nJ) and can span a high dynamic range [31]. Compared to third order nonlinear processes, the disadvantages of this technique are an unambiguously defined time axis and rather unintuitively looking traces.

As part of this thesis, the setup of a SHG FROG, which can be seen in figure 2.5, was optimized, regarding alignment and measurement time. The beam enters the setup at the bottom right of the figure through a pinhole. It is split in two by a D-shaped mirror (D) to have the same amount of dispersion in each arm. The reflected beam is sent to a manually moveable delay stage, which is used for coarse adjustment of the temporal overlap. The other part goes to a piezo-driven stage. With this stage, the delay between the two pulses is varied stepwise over one measurement with a maximum range of ≈ 2 ps (320 μ m scan range). With a parabolic mirror, both beams are focused in a 10 μ m thick Beta-Barium-Borate (BBO) crystal. In this noncollinear setup, there is SH signal between the two fundamental beams, which is caused by the temporal and spatial overlap of the pulses, in addition to the signals in the individual arms. As a result, the signal that is caused by this gating mechanism, can be easily separated from the collinear SH paths. The spatial overlap is found by placing a camera in the

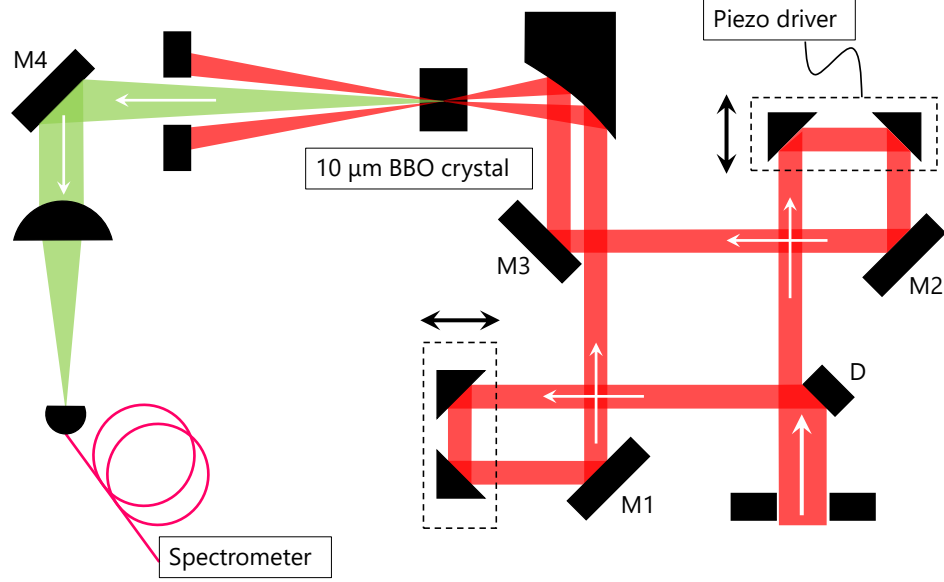


Figure 2.5: Setup of an SHG FROG. The beam enters through a pinhole at the bottom right of the figure and is split in two with a D-shaped mirror. The noncollinear SH signal, generated in a $10\ \mu\text{m}$ thick BBO crystal, is measured with a spectrometer as a function of the delay between the two beams.

focus of the parabolic mirror and adjusting either mirror M2 or M3. There is a second pinhole behind the crystal for aligning the incoming beam to the FROG and blocking the collinear SH beams. The SH beam is focused into a multi mode fibre which is connected to a Blue Wave Spectrometer from StellarNet.

For the SHG FROG, the spectrally resolved signal field $E_{\text{signal}} = E(t)E(t-\tau)$ produces the interferogram [31]:

$$I_{\text{FROG}}^{\text{SHG}}(\omega, \tau) = \left| \int_{-\infty}^{\infty} E(t)E(t-\tau)e^{-i\omega t} dt \right|^2 \quad (2.18)$$

Here, $E(t)$ and $E(t-\tau)$ are the electric fields of the two replica of the input pulse. From this spectrogram, the electric field, spectrum and phases are calculated via the concept of generalized projections [38], which is the following: There are two constraints, that

the signal field has to fulfill: Firstly, it can be generated from a physically possible field $E(t)$ via SHG. Secondly, it produces the measured FROG trace. The intersection of these two sets of functions gives the result of the measurement. This can be reached by alternately projecting the retrieved data onto the two sets of functions until the algorithm converges [39]. For example, Rick Trebino's group provides a code (see frog.gatech.edu/code.html) that retrieves the spectra, fields and phases from the raw trace. The convergence criterion for the retrieval process is the FROG error, which is given by the following equation, namely the difference between the measured and retrieved spectrogram for each combination of ω and τ [32]:

$$G = \sqrt{\frac{1}{N^2} \sum_{i,j=1}^N \left| I_{\text{FROG}}(\omega_i, \tau_j) - \alpha I_{\text{FROG}}^{(k)}(\omega_i, \tau_j) \right|^2} \quad (2.19)$$

The variable α is used to minimize the error, k indicates the recent iteration and I_{FROG} and $I_{\text{FROG}}^{(k)}$ are the measured and retrieved points of the spectrogram, respectively. As this error scales with $\frac{1}{N}$, it is not directly comparable for FROG traces with different grid sizes. Furthermore, as the FROG trace consists of N^2 points, from which only $2N$ points have to be calculated (N for the spectrum/field and N for the phase), the measurement is drastically oversampled. Therefore, if the algorithm converges, it is very likely that the solution corresponds to the actual field and phase. Nevertheless, it is in principle possible, that two different pulses lead to the same FROG trace and that the retrieved data does not correspond to the actual pulse. Therefore, it is very important to specify the FROG error mentioned above and to make the following consistency checks:

It can be checked using the marginals, whether the acquired trace corresponds to the pulse that should be measured. This means, calculating the integral of the FROG trace over the delay or frequency axis and comparing it to the autoconvolution of the input spectrum or an independently measured AC, respectively. These have to agree and disagreement would correspond to a systematic error in the trace acquisition. The retrieved data can be validated by comparing the retrieved spectrum with an independently measured one or the AC calculated from the retrieved field with an independently measured AC.

For the retrieval, it is important to sample the trace properly. Most importantly, all non-zero FROG data has to lie within the preferably quadratic grid. Furthermore there are two limits to the data sampling rate. As the dimensions of the grid are related via a FT, the time step size Δt is proportional to the inverse full width in ω . Therefore, Δt has to be chosen small enough, that the data does not go off the grid in frequency direction. Secondly, it has to be large enough that the data does not go off the trace on the delay axis for a given grid size N . In conclusion, one should consider the minimum time stepsize first and chose a grid size afterwards which does not truncate the trace. A small grid might make the retrieved spectra and fields look jagged, yet no information is lost if the resolution is high enough. The data may be smoothed by adding artificial zeros to the outer parts of the trace, but no information is gained by that [31, 40].

As the SHG is a second order process, the traces are symmetric in time, meaning that $E(t)$ (with the phase $\phi(t)$) and $E(-t)$ (phase $-\phi(t)$) result in the same FROG trace. Therefore, no unique time direction can be defined from one single measurement. This ambiguity can be solved by placing a piece of glass in the beam path or removing a certain amount of GDD from the beam path and acquiring another FROG trace. The curvature of the phase of the second trace is then unambiguously known. One can then either compare unique features in the phase that are caused by spectral modulations and determine the correct time direction that way. Another possibility is the mathematical subtraction or addition of the known GDD to the phase retrieved from the first measurement. Only one time direction will lead to the same result as the second measurement.

With the FROG setup described above, broadband pulses with durations below 20 fs should be measured. Therefore, phase matching of the fundamental and the SH in the nonlinear crystal has to be considered. The SH intensity I_{SH} for a crystal of length L is proportional to:

$$I_{\text{SH}}(L) \propto \omega_0^2 L^2 \text{sinc}(\Delta k L / 2) \quad (2.20)$$

where ω_0 is the input frequency and Δk the phase mismatch. This is caused by

the different propagation velocities of the two beams through the crystal. For the noncollinear FROG configuration described above it is given by:

$$\Delta k = k_{\text{fund}} \cos(\Theta/2) + k_{\text{fund}} \cos(\Theta/2) - k_{\text{SH}} \quad (2.21)$$

with Θ being the angle enclosed by the two incoming beams. The wave numbers of the fundamental and the SH beam are denoted as k_{fund} and k_{SH} , respectively. Inserting the dispersion relation $k(\omega) = \frac{\omega n_{\text{R}}(\omega)}{c}$ (refractive index $n_{\text{R}}(\omega)$) in equation 2.21 leads to:

$$\Delta k = \frac{2\omega}{c} [n_{\text{fund}} \cos(\Theta/2) - n_{\text{SH}}] \quad (2.22)$$

with the refractive index n_{fund} for the fundamental beam and n_{SH} for the SH. The FROG setup described above uses type I phase matching, meaning that the fundamental is chosen to be the ordinary and the SH the extraordinary beam in the birefringent BBO crystal. Perfect phasematching ($\Delta k = 0$) can be reached for one wavelength, but never for the whole spectral bandwidth of a very short pulse. The phasematching bandwidth drops with the crystal length L , whereas the intensity of the second harmonic scales as L^2 . Therefore a trade-off between signal strength and phase matching bandwidth has to be found [31]. Figure 2.6 shows the relative signal strength as a function of wavelength for noncollinear SHG in a 10 μm BBO crystal for three different angles between the fundamental beams. For a small crossing angle, the phasematching bandwidth is narrower, but the efficiency can be higher, whereas the bandwidth increases for higher crossing angles with the disadvantage of lower overall efficiencies. In the setup described above, the angle is about 15° , leading to a fairly uniform efficiency over the whole considered spectrum from 950 nm to 1175 nm.

Furthermore, spatial chirp that can be caused, for example, by a misalignment of pulse stretchers or compressors, can distort the FROG trace. As the beam is split in two by a D-shaped mirror, only a spatially homogeneous beam can lead to a perfectly symmetric trace. This makes asymmetric traces a good indicator for spatial chirp, which can then be removed, by realignment of the optical elements. In the case of single shot FROG or GRENOUILLE, spatial chirp can be directly seen in the shape of the trace and therefore also quantified to some extent [41]. It should also be considered, that only the central part of the signal carries signal from the delay caused by the stage,

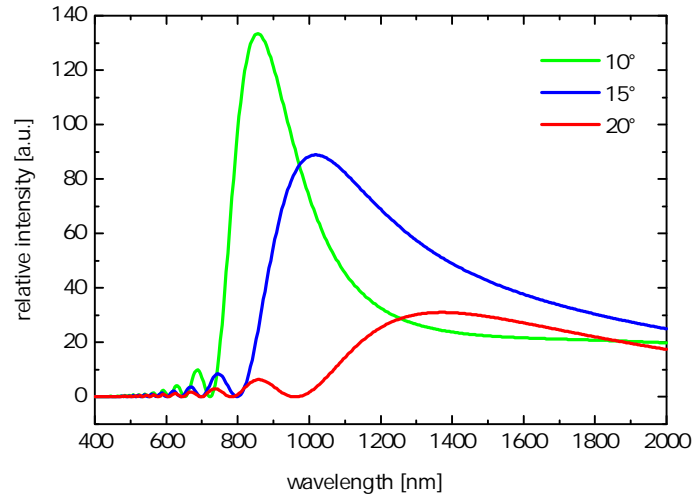


Figure 2.6: Phase matching efficiency for noncollinear SHG in a $10\ \mu\text{m}$ thick BBO crystal for different crossing angles of the fundamental beams.

the outer parts are geometrically delayed. This 'geometric smearing', which is used in GRENOUILLE measurements, is important for single cycle pulses. There, it can be removed with a pinhole that cuts out the central part of the signal beam, or by reducing the slit size of the spectrometer [31].

In order to make measurements of the intracavity pulses in a locked cavity possible, we had to drastically reduce the measurement time with our FROG apparatus, because the lock was only stable on the order of tens of seconds. With an analogous readout of the piezo stage position, we could improve the acquisition time for a trace of ≈ 300 points from several minutes to ≈ 10 s. With lower time resolution, this makes quasi-live optimization of the pulse duration possible.

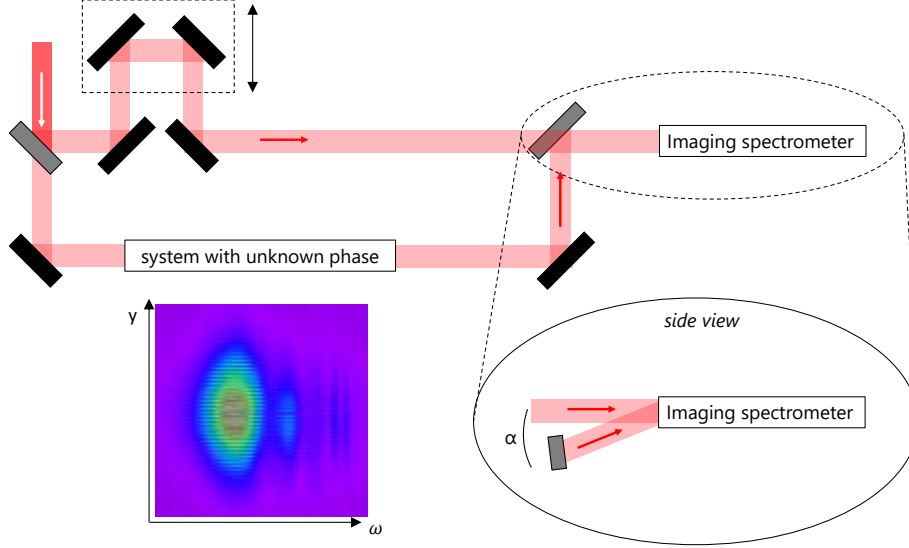


Figure 2.7: Setup of the SSI measurement. The upper part of the figure shows the top view of the beam path. At the beginning, the beam is split in two. The reference beam goes to a delay stage and directly to the imaging spectrometer. The SSI beam passes the system with unknown phase. At the imaging spectrometer, the beams are overlapped with an angle α inbetween, which can be seen in the side view. This produces the inset interferogram as a function of spatial coordinate y and frequency ω .

2.3.2 Spatial Spectral Interferometry (SSI)

SSI can be used for measuring the unknown spectral phase of a system, like a mirror or an EC with respect to a reference beam [15, 21, 37]). The schematic setup is shown in figure 2.7.

The beam is split into two with a beam splitter. One part (reference beam) directly goes to the imaging spectrometer via a delay stage for temporal synchronization of the laser pulses. The other part goes through the system with unknown phase - like for example an EC or mirror multipass setup - and then to the spectrometer. At the spectrometer, the two beams are overlapped under an angle α . The resulting interferogram $I(y, \omega)$ in spatial direction y and frequency ω is given by [37]:

$$I(y, \omega) = I_R(y, \omega) + I_S(y, \omega) + 2\sqrt{I_R(y, \omega)I_S(y, \omega)} \cos \left[\phi(\omega) + \omega\Delta\tau + y\frac{\omega}{c} \sin(\alpha) \right] \quad (2.23)$$

Here, I_R and I_S are the interferograms of the reference (R) and SSI (S) beams respectively, which can be measured independently. The modulation in the interferogram in y and ω is given by the relative phase $\phi(\omega)$ between the two beams, the time delay $\Delta\tau$ and the sine of the angle α . If $\Delta\tau = 0$, a cosine fit in y for each ω has the phase $\phi(\omega)$ as an offset. The delay is set to zero when the interference fringes are horizontal. In comparison to spectral interference, where the relative phase is calculated from only one frequency dependent oscillation pattern, SSI provides increased spectral resolution, because no spectral filtering is necessary [42–44].

Together with an EC, SSI can be used for highly sensitive phase measurements, because of the increased number of passes on the used mirrors or an increased interaction length with a medium [37].

Chapter 3

Experiments

In the frame of this thesis, work on two experiments was performed. Firstly, we built an ultrabroadband EC and demonstrated an intracavity pulse duration below 20 fs for the very first time. To do so, mirrors with matching dispersion had to be coated and characterized, and methods for the intracavity pulse characterization had to be found. Secondly, we used narrowband input pulses and placed a 100 μm FS substrate in the cavity focus. We demonstrated coherent intracavity spectral broadening in that substrate and are currently developing methods for compressing the pulses and investigating their applicability for spectroscopy.

3.1 Ultrabroadband linear enhancement cavities

As described in section 2.2, an EC leads to both intensity and sensitivity enhancement. The latter can be exploited for spectroscopy but is a limiting factor when ultrashort pulses should be coupled to the cavity. This is due to the sensitivity of the cavity to the phase of the used mirrors, which should ideally be only linear in order to effectively couple the complete frequency comb to the cavity (see section 2.2). State-of-the-art pulse parameters for the broadest possible ECs before our experiments were 30 – 35 fs with an average powers 3.3 – 10 kW, shown in [21] and [45]. This corresponds to a maximum spectral width of 100 nm at -10 dB.

In the experiment reported here, we measured sub-20-fs pulses with a bandwidth of > 150 nm in a high-finesse ($\mathcal{F} = 340$) EC with an average power around 1 kW for the very first time [46]. Firstly, we characterized the potential cavity mirrors to find out

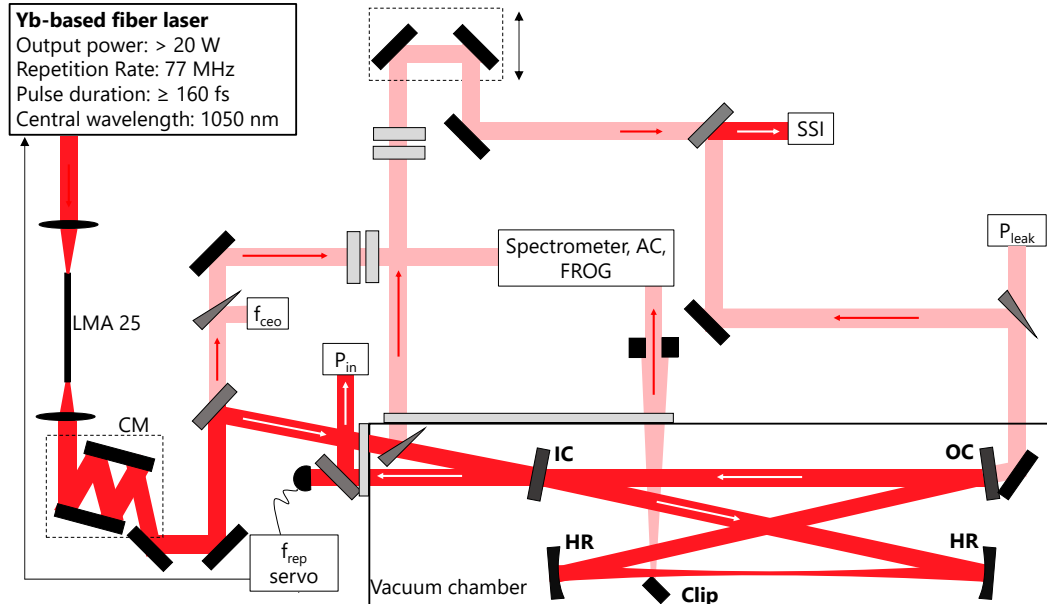


Figure 3.1: Setup for the ultrabroadband EC experiment. Starting at the top left with the Yb-based fiber laser described in [48], the pulses are then spectrally broadened in a Large-Mode-Area (LMA) fibre and compressed with CMs. The beam is then sent to the EC. Some power, split off with a wedge, is used for diagnostics with spectrometer, FROG, AC and SSI and locking the cavity. A D-shaped mirror is inserted in the beam path for directly measuring the intracavity spectra and pulses with a spectrometer and FROG.

whether their phase is flat enough for the use in the cavity. Secondly, we found two methods for characterizing the intracavity pulse. Finally we could demonstrate intracavity pulses with the mentioned parameters, which pave the way to the generation of isolated attosecond pulses [13, 14, 47], or broadband, cavity-enhanced stimulated Raman spectroscopy [16]. Furthermore, the cavity has an optimum CE offset frequency of half the repetition rate, which makes this mirror combination suitable for field sensitive experiments like HHG in a cavity [25].

3.1.1 Setup

At the beginning of this thesis, the laser had already been set up as it is shown in figure 3.1.

The setup starts with the Yb-based fibre laser described in [48], with a used output

power of 16 W, a repetition rate of 77 MHz and a minimum pulse duration of 160 fs with the spectrum centered around 1047 nm. The pulses are then sent to a LMA25 (LMA = Large Mode Area) fibre for spectral broadening via SPM [49] and compressed with several passes on CMs [50] down to 20 fs. One part of the beam is sent to a f-2f interferometer for monitoring the f_{ceo} , which can be coarsely adjusted with an Acousto-Optic-Modulator (AOM), that varies the losses in the oscillator. Spectrum, AC and FROG of the input pulse can be measured in a beam split off with a wedge. For the FROG measurement, two FS substrates are placed in the beam path to account for the phase of the vacuum chamber window and the IC, that the pulse passes before the cavity. With another beamsplitter, the reference arm for the SSI is split off before the IC. Two FS substrates again account for the additional dispersion in the cavity arm. The remaining power is sent to the cavity, where the reflection off the IC is used for locking the laser to the cavity by adjusting its repetition rate with the Pound-Drever-Hall locking scheme [51]. Furthermore, the input power is measured in the reflected beam when the cavity is far from resonance with the laser. The leakage through the fourth cavity mirror is sent to the SSI as the sample arm. To measure the FROG and the intracavity spectrum, a D-shaped mirror with a sharp edge is inserted into the beam path without noticeably increasing the cavity losses. The central part of the clipped beam is cut out with a pinhole for spatial shaping. The cavity is placed in a vacuum chamber with a pressure of about 10^{-2} mbar, to avoid the dispersion of air.

Measurement of the intracavity power

For the measurement of the intracavity power, a beamsplitter was placed in the transmission through the IC that goes to the SSI, to send some of the leakage power to a powermeter. The overall transmission from the cavity to the powermeter around 1050 nm was measured to be $340 \cdot 10^{-6}$. With this value, we normalized the IC transmission data $T(\lambda)$ which can be seen in figure 3.2. We have to consider the shape of the IC transmission curve, because of its nonuniformity. Otherwise, especially the increased transmission at the outer ranges of the spectrum would distort the power measurement.

With the intracavity spectrum $S_{\text{cav}}(\lambda)$ and the measured leakage power P_{leak} , the circulating power can be calculated with equation 3.1.

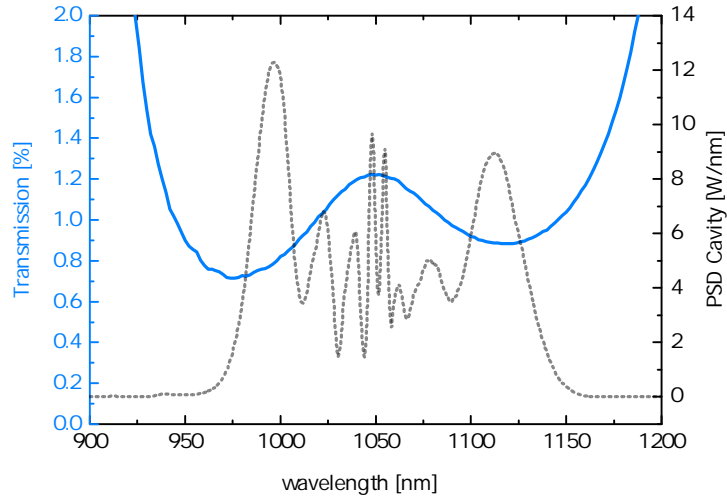


Figure 3.2: IC transmission data, used for calculating the intracavity power from the power leaking through the second cavity mirror. Dotted line: typical intracavity spectrum.

$$P_{\text{circ}} = P_{\text{leak}} \frac{\int S_{\text{cav}}(\lambda) d\lambda}{\int S_{\text{cav}}(\lambda) T(\lambda) d\lambda} \quad (3.1)$$

For one complete parameter set, we measured the input and intracavity spectrum with an OSA. Furthermore, we acquired a FROG trace of the input and intracavity pulse and measured the phase of the cavity with SSI. We measured P_{leak} , the input power and the power reflected off the input coupler in the locked state (P_{refl}).

3.1.2 Characterization of the cavity mirrors

Before setting up the cavity, a set of mirrors, that supports the 20-fs input pulses, had to be chosen. As the production of mirrors with a flat phase over a broad bandwidth with the accuracy needed for the use in an EC is at the limit of what is possible with state-of-the-art coating techniques, this is no straightforward process. Variations in layer thicknesses on the scale of a few nanometers can drastically influence the phase and make the mirrors unsuitable for the cavity. Therefore we measured the mirror phase with SSI in a multipass setup with a sensitivity of < 5 mrad (see in detail in [46]). The setup is sketched in figure 3.3.

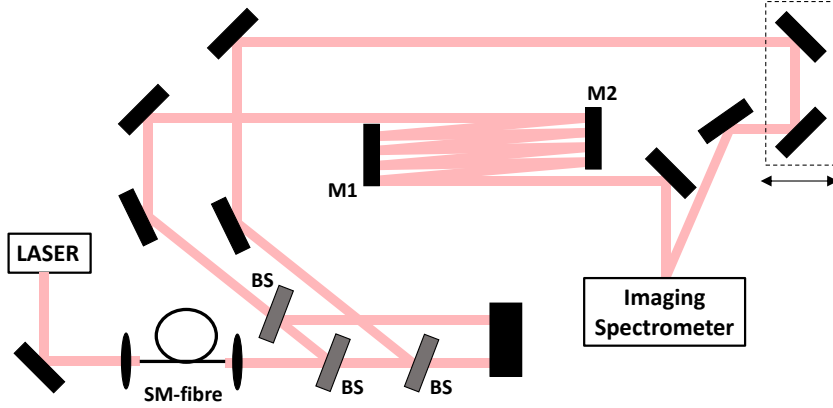


Figure 3.3: Multipass-SSI-setup for sensitive measurement of the phase of the mirrors M1 and M2. The laser beam is spatially filtered in the Single-Mode (SM) fibre. The beamsplitter (BS) configuration ensures the same amount of dispersion in the reference and sample arm. The beam is folded on the two mirrors M1 and M2 as such, that it makes 24 passes in total. The beams are then overlapped in the Imaging Spectrometer as described in section 2.3.2.

The laser beam (described in section 3.1.1) is spectrally filtered in a single-mode fibre after the CM compression. The beamsplitter configuration ensures the same amount of dispersion in both the reference and sample arm. The beam is folded to make in total 24 passes on the mirrors (M1, M2), the phase of which should be measured. For the phase measurement, the beams are overlapped in the imaging spectrometer, as described in section 2.3.2 for the SSI-measurement. The left part of figure 3.4 shows the results of this measurement for the final cavity mirrors, in comparison with the designed mirror phases.

It can be clearly seen that the measured phases deviate from the designed ones significantly. Luckily, they are curved oppositely and can therefore partially compensate for each other. As we were setting up a four mirror cavity, we searched for the mirror combinations from this coating run with the flattest phase. Two possible combinations can be seen in the right part of figure 3.4. The first mirror combination consists of three HR mirrors and one IC (IC limited cavity). The other one is an impedance matched cavity, consisting of two HR mirrors and two ICs. Figure 3.4 also shows the π/F corridor mentioned in section 2.2 as the limit of acceptable phase distortions.

The phase of the IC-limited cavity is clearly curved and significantly exceeds the π/F

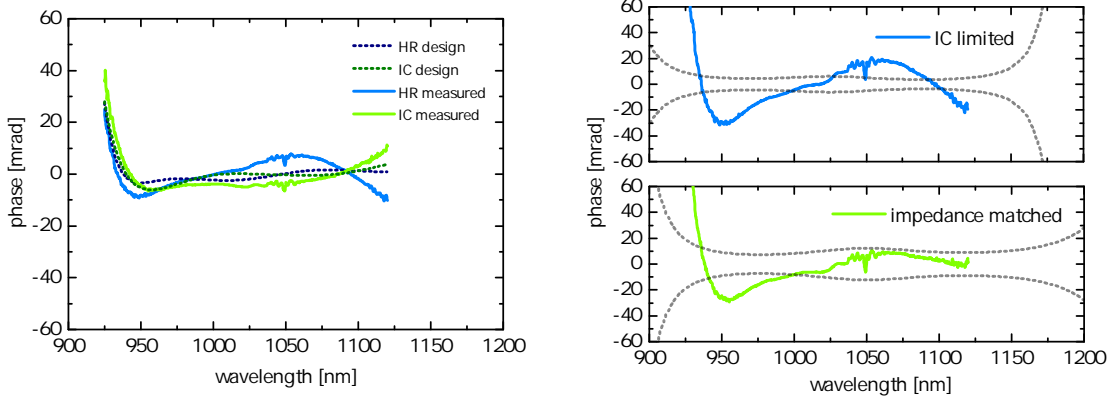


Figure 3.4: Left: Designed and measured single mirror phase of the HR mirrors and ICs. The solid lines show the phases measured with multipass SSI, the dotted ones are the designed mirror phases. Right: Phases of possible mirror combinations for the ultrabroadband cavity (roundtrip phase). Upper panel: IC limited cavity, consisting of three HR mirrors and one IC. Lower panel: impedance matched cavity, consisting of two of each mirrors. Dotted lines: π/F corridor of phase distortions that would cause an enhancement drop to 1/2 of the maximum enhancement.

corridor, making this combination unsuitable for the sub-20-fs cavity. In the case of the impedance-matched cavity combination, the corridor is broader and the phase curvature smaller. There is still some GDD (-1.2 fs^2) left, but it can be compensated with 24 mbar of air or $40 \mu\text{m}$ FS. As a proof of principle, we chose to build up the impedance-matched cavity and adjust the GDD by raising the intracavity air pressure to 24 mbar.

3.1.3 Results: Cavity Bandwidth

Measurements of the empty cavity

The left part of figure 3.5 shows the input and intracavity spectrum without gas in the cavity.

The intracavity spectrum is about $\Delta\lambda_{\text{FWHM}} = 158 \text{ nm}$ broad and its FT limit is $\Delta t_{\text{FWHM}} = 17.5 \text{ fs}$. We calculated the intracavity power to be 952 W from equation 3.1. The average power enhancement was $E = 70$ with a finesse of $\mathcal{F} = 338$. The OOF to reach these parameters was 38.5 MHz , which corresponds to half the laser rep-

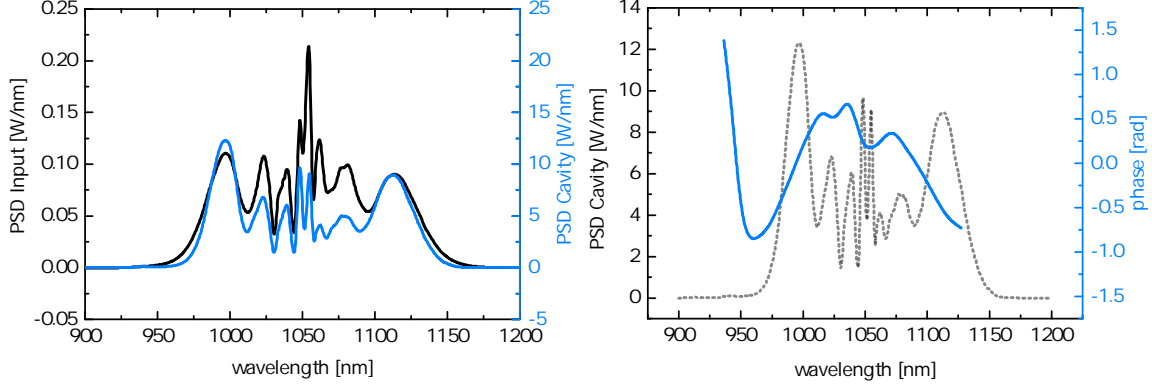


Figure 3.5: Left: Input and intracavity spectrum of the empty cavity. The spectral width of the intracavity spectrum is $\Delta\lambda_{\text{FWHM}} = 158$ nm, which corresponds to a FT limit of $\Delta t_{\text{FWHM}} = 17.5$ fs. Right: Phase of the empty cavity, measured with SSI. Dotted line: intracavity spectrum. PSD: Power Spectral Density

etition rate. This makes the mirror combination suitable for field sensitive intracavity experiments like HHG [25].

Measurements with 24 mbar air in the cavity

For the measurement with 24 mbar of air in the cavity, we broadened the input spectrum by changing the compression of the pulses before the nonlinear fibre. This caused a negative chirp of the input pulses that was not compensated in these experiments. The input and intracavity spectra for that case can be seen in the left part of figure 3.6.

The width of the intracavity spectrum is $\Delta\lambda_{\text{FWHM}} = 183$ nm, and its FT limit is $\Delta t = 15.7$ fs. We calculated the circulating power to be 1043 W at a finesse of $\mathcal{F} = 340$. The enhancement $E = 77$ was a little bit higher than without gas. This is due to the better matching of the input comb to the cavity resonances, caused by the flatter cavity phase, which can be seen in the right part of figure 3.6.

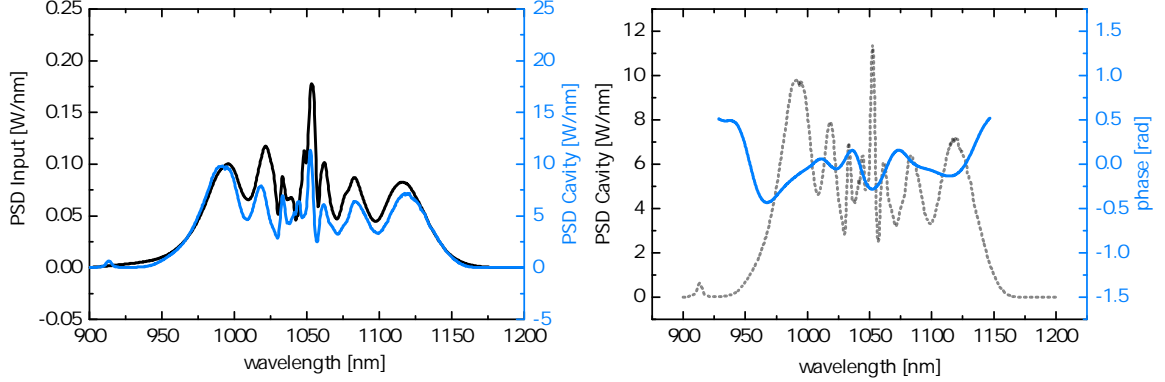


Figure 3.6: Left: Input and intracavity spectrum with 24 mbar of air in the cavity. The spectral width of the intracavity spectrum is $\Delta\lambda_{\text{FWHM}} = 183$ nm, corresponding to a FT limit of $\Delta t = 15.7$ fs. Right: Cavity phase with gas in the cavity, measured with SSI. Dotted line: intracavity spectrum.

3.1.4 Characterization of the intracavity pulse

The characterization of the intracavity pulse should be done without affecting the cavity properties. We found two different methods, the results of which are in good agreement. Method one is the measurement of the input and cavity phase with FROG and SSI, respectively. The intracavity spectrum is measured independently and the intracavity pulse can then be calculated. Method two is the direct measurement of the intracavity pulse with a clipped beam, produced by inserting a D-shaped mirror in the cavity beam path.

Measurement of the input pulse

In method one, the input pulse (spectrum $S_{\text{in}}(\omega)$ and spectral phase $\phi_{\text{in}}(\omega)$) is sent to the SHG FROG described in section 2.3.1. We put 12 mm of FS in the beam path before the FROG to account for the vacuum chamber window and the IC that the beam passes before circulating through the cavity. For the unambiguous determination of the time direction of the FROG measurement, a FROG trace without the two FS substrates was acquired, which is clearly negatively chirped. The correct time direction can then be found as described in section 2.3.1. We measure the cavity phase ($\phi_{\text{SSI}}(\omega)$) with respect to the input beam with SSI (see section 2.3.2). As a result, the total phase

of the pulse in the cavity is given as the sum $\phi_{\text{cav}}(\omega) = \phi_{\text{in}}(\omega) + \phi_{\text{SSI}}(\omega)$. The intracavity spectrum $S_{\text{cav}}(\omega)$ is measured in the clipped beam with an optical spectrum analyzer (OSA). The intracavity pulse in the time domain, $E(t)$, can then be calculated via the FT:

$$E(t) = \int_{-\infty}^{\infty} S_{\text{cav}}(\omega) e^{-i\phi_{\text{cav}}(\omega)} e^{i\omega t} d\omega \quad (3.2)$$

Measurement of the intracavity pulse

For the direct intracavity pulse measurement, we inserted a D-shaped mirror into the beam path with a motorized stage. We checked in the cavity scan and by calculating the average power enhancement, that the losses were not increased noticeably. The light reflected off the clipping mirror is then sent to the FROG. The phase of $d_{\text{FS}} = 6$ mm FS has to be subtracted from the retrieved phase ϕ_{FROG} , because the pulses pass a vacuum chamber window before the FROG. This phase ϕ_{FS} is given by equation 3.3.

$$\phi_{\text{FS}} = k(\omega)d_{\text{FS}} = \frac{n_{\text{FS}}(\omega)\omega d_{\text{FS}}}{c} \quad (3.3)$$

The refractive index $n_{\text{FS}}(\omega)$ can be calculated from Sellmeier's equation for FS with λ given in μm as [18]:

$$n_{\text{FS}}(\lambda) = \sqrt{1 + \frac{0.6961663\lambda^2}{\lambda^2 - 0.0684043^2} + \frac{0.4079426\lambda^2}{\lambda^2 - 0.1162414^2} + \frac{0.8974794\lambda^2}{\lambda^2 - 9.896161^2}} \quad (3.4)$$

The correct time direction of the FROG measurement can be determined from method one. As the intracavity pulse from that measurement is positively chirped and the vacuum chamber window only adds positive GDD, the retrieved phase of the second method also has to have a positive curvature in the frequency domain.

The losses caused by clipping the beam are strongly dependent on the position of the D-shaped mirror in the beam path and are not the same for all wavelengths, because of the wavelength dependent beam size described in section 2.2. As the losses vary with wavelength, so does the enhancement. The dependencies of both these parameters on the clipping position are depicted in figure 3.7 for three different wavelengths.

The further at the edge the beam is clipped, the lower the losses are, but the stronger

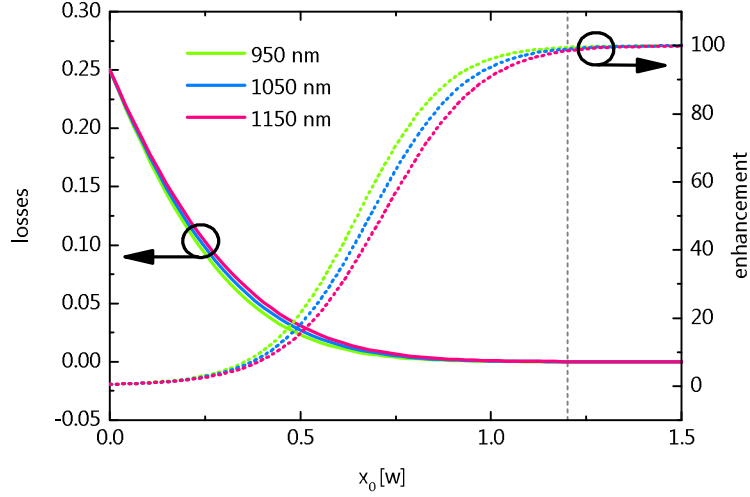


Figure 3.7: Cavity losses and enhancement as a function of clipping mirror position in units of the beam radius. The dotted line indicates the regime we worked in during the pulse duration measurements.

their relative wavelength dependency gets. A less wavelength dependent way of accessing the intracavity beam would be using a pierced mirror, as the wavelength dependence is less in the center of the beam. This method was used for the outcoupling of the high harmonics that were produced in a gas target inside an enhancement cavity, for example in [45]. There, the lower divergence of the lower wavelengths was exploited.

For the intracavity FROG measurements in the following chapter, we did not see a change in enhancement, when the clipping beam was in the beam path. Therefore, we assumed the overall losses A_{clip} caused by the D-shaped mirror to be around 10^{-4} (from figure 3.7). This corresponds to a clipping position of $x_0 = 1.2 w$ from the beam centre, calculated by solving equation 3.5 for x_0 .

$$A_{\text{clip}} = \left(\frac{\int_{x_0}^{\infty} e^{-2x^2/w^2(\omega)} dx}{\int_{-\infty}^{\infty} e^{-2x^2/w^2(\omega)} dx} \right)^2 \quad (3.5)$$

The ratio of the clipping to the total beam size has to be squared, as not only losses are introduced by the reflection of part of the beam outside the cavity, but the spatial

overlap of the intracavity beam and the input beam is reduced by the same factor [52]. With known x_0 , the frequency distribution in the clipped beam can be calculated as:

$$I(\omega) = \int_{-\infty}^{\infty} e^{-2y^2/w^2(\omega)} dy \cdot \int_{x_0}^{\infty} e^{-2x^2/w^2(\omega)} dx \quad (3.6)$$

We tilted the retrieved FROG spectrum $S_{\text{FROG}}(\omega)$ according to this distribution, resulting in the true intracavity spectrum of the complete beam. This is reasonable, as the clipped beam still consists of the complete spectrum and therefore no phase information is lost. As a consequence, the FROG trace is tilted, but the retrieved phase is not changed by the spectral tilt. The intracavity pulse in the time domain is then given by the following FT:

$$E(t) = \int_{-\infty}^{\infty} \frac{S_{\text{FROG}}(\omega)}{I(\omega)} e^{-i(\phi_{\text{FROG}} - \phi_{\text{FS}})} e^{i\omega t} d\omega \quad (3.7)$$

3.1.5 Results: Intracavity pulse duration

In the following, the results for the intracavity pulse characterization with the two methods described in section 3.1.4 will be presented. We did this both for the empty cavity and for the one filled with 24 mbar of air.

Measurements of the empty cavity

Figure 3.8 shows the measured and retrieved FROG traces of the input pulse with and without 12 mm of FS in the beam path.

The FROG error was $G = 0.008$ and $G = 0.014$, respectively, for a grid size of 512×512 pixels. The retrieved spectral phases of the two measurements are compared in figure 3.9.

The pulse without FS has to be negatively chirped, as it is close to the FT limit otherwise. After mathematically adding the phase of 12 mm FS, it only corresponds to the measured one for one time direction. The retrieved input field has a FWHM pulse duration of 19.4 fs. We measured the cavity phase with SSI, which can be seen in the right part of figure 3.5. It varies by ± 1 rad around 0, which corresponds to a roundtrip phase of ± 3 mrad when divided by the cavity finesse.

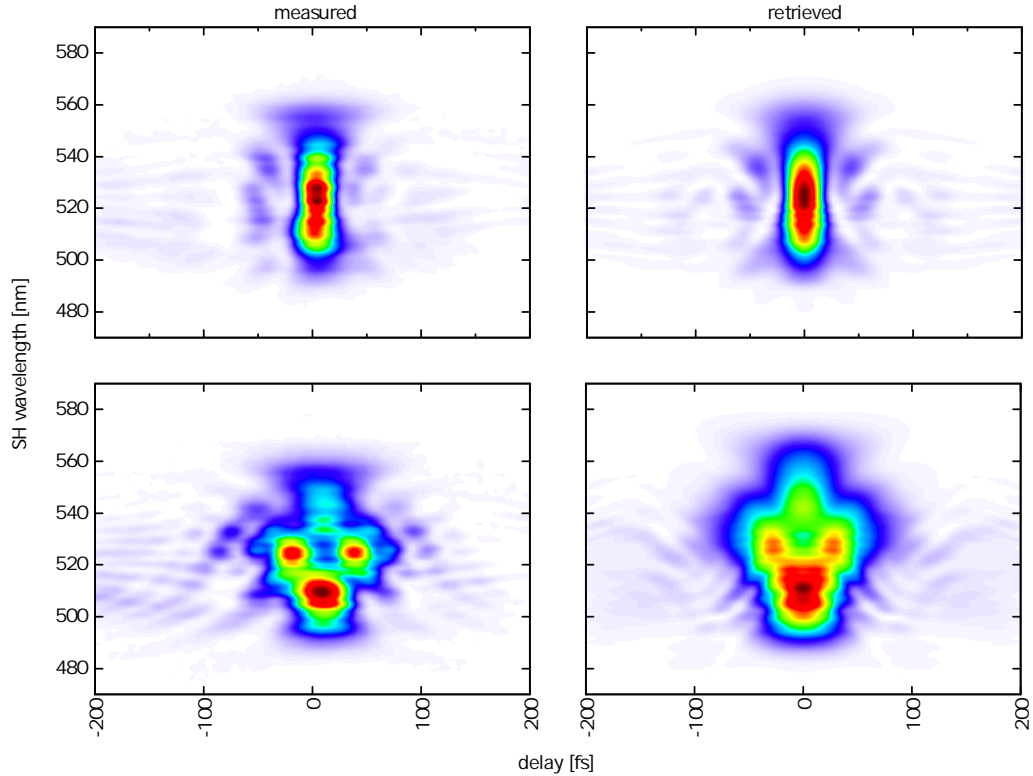


Figure 3.8: Measured and retrieved SHG FROG traces for the input pulse with (upper row) and without (lower row) 12 mm FS in the beam path. The FROG error was $G = 0.008$ and $G = 0.014$ respectively (grid size: 512×512 pixels).

The intracavity spectrum and field, together with the respective phase, resulting from method one (equation 3.2) can be seen in figure 3.11.

The FROG traces measured directly from the clipped beam for the second method of pulse duration determination are shown in figure 3.10.

The FROG error was $G = 0.005$ for a grid size of 512×512 pixels and the retrieved pulse duration was 20.5 fs. As described in section 3.1.4, the phase of the vacuum chamber window has to be subtracted from the phase retrieved from that trace in order to get the real intracavity pulse. Both the retrieved and vacuum chamber window phase can be seen in the right part of figure 3.9.

We tilted the retrieved spectrum with the wavelength dependent intensity distribution

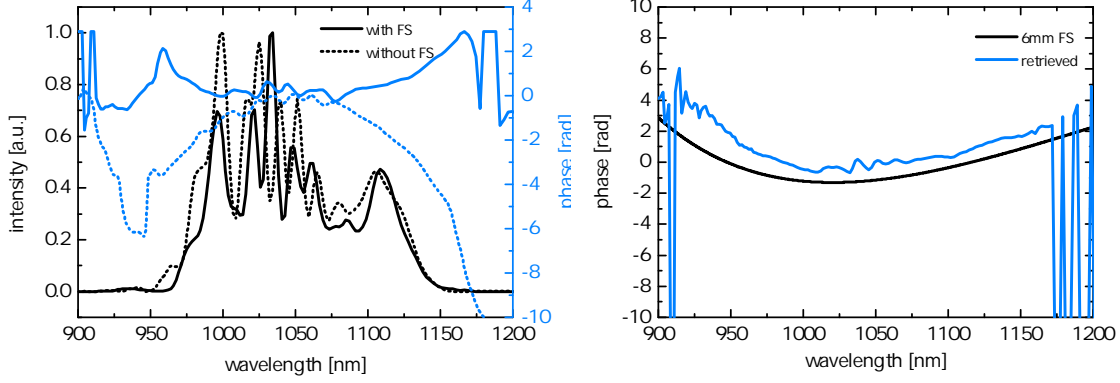


Figure 3.9: Left: Retrieved spectrum and spectral phase with (solid) and without (dotted) 12 mm FS in the beam path. Right: Phase retrieved from the intracavity FROG measurement (blue) and phase of 6 mm FS (black).

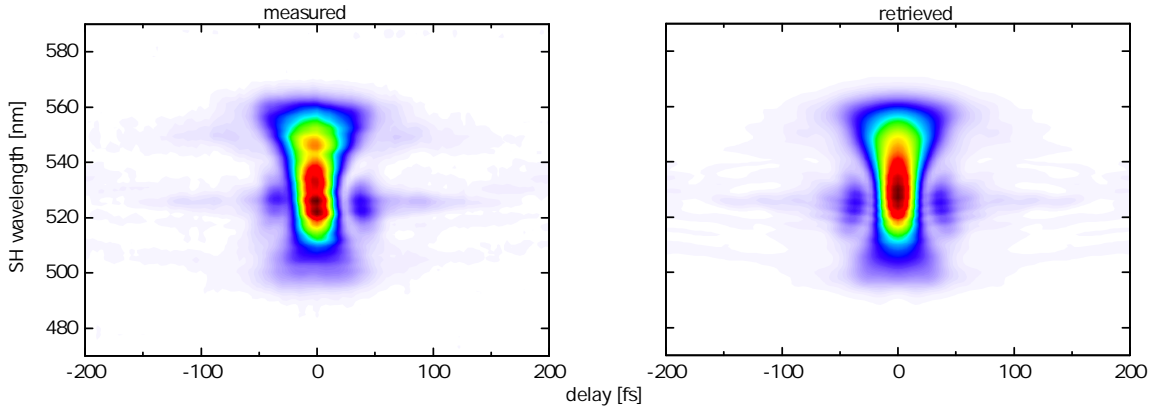


Figure 3.10: Measured and retrieved FROG trace of the intracavity pulse, measured with the clipped beam. The FROG error was $G = 0.005$ for a grid size of 512×512 pixels.

of the clipped beam from equation 3.6. The final results for spectrum, field and the respective phases can be seen in figure 3.11 (“Method 2”), together with the results from method one.

The pulse duration calculated with method one is 19.0 fs and 18.8 fs with method two, corresponding to about 5.4 cycles of the electric field. One can clearly see from figure 3.11, that the spectral and temporal shapes retrieved from both methods show excellent agreement.

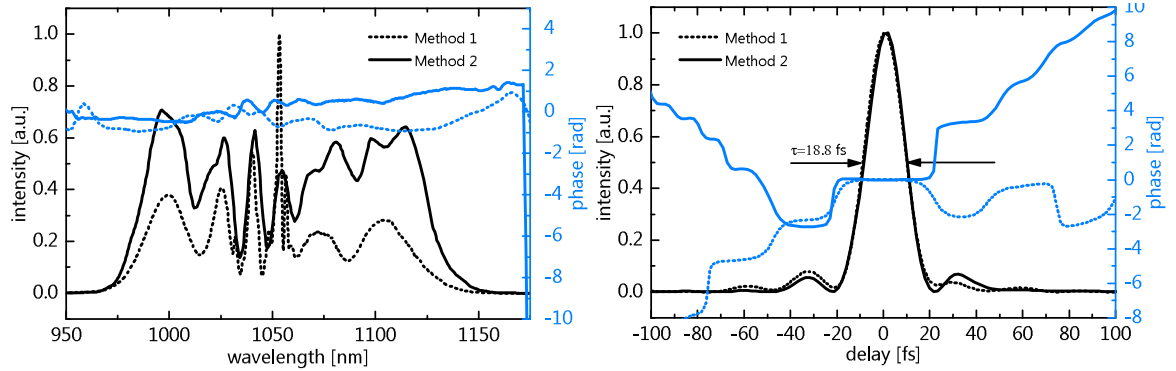


Figure 3.11: Intracavity spectra (left) and fields (right) with (spectral) phases. Dotted lines: Method 1 (input measurement). Solid lines: Method 2 (direct intracavity measurement). The pulse duration calculated from Method 1 is $\Delta t_{\text{FWHM}} = 19.0$ fs and 18.8 fs from Method 2.

Measurements with 24 mbar air in the cavity

The FROG traces for both the input (FROG error $G = 0.013$) and intracavity measurements (FROG error $G = 0.005$) can be seen in figure 3.12 (both with a grid size of 512×512 pixels).

For the intracavity measurement, we assumed the pulse to be negatively chirped at the FROG, because the negative chirp of the input pulse was higher than the positive GDD of the chamber window.

Figure 3.13 shows the resulting intracavity spectra and fields and their respective phases. The pulse durations in this case are 24.6 fs for the input and 25.5 fs for the intracavity measurement, corresponding to about 7.5 cycles of the electric field.

For this measurement, the agreement between the two techniques is quite good in the frequency domain. Furthermore, the resulting intracavity pulse durations differ by < 1 fs, although the pulse shapes show some differences.

In conclusion, we measured intracavity pulses with a pulse duration below 20 fs and an average power of 952 W in a high finesse ($\mathcal{F} = 338$) cavity. We could reach an even broader intracavity spectrum by inserting 24 mbar of air in the cavity, thus increasing the intracavity power to 1043 W. In this case, the dispersion compensation was not

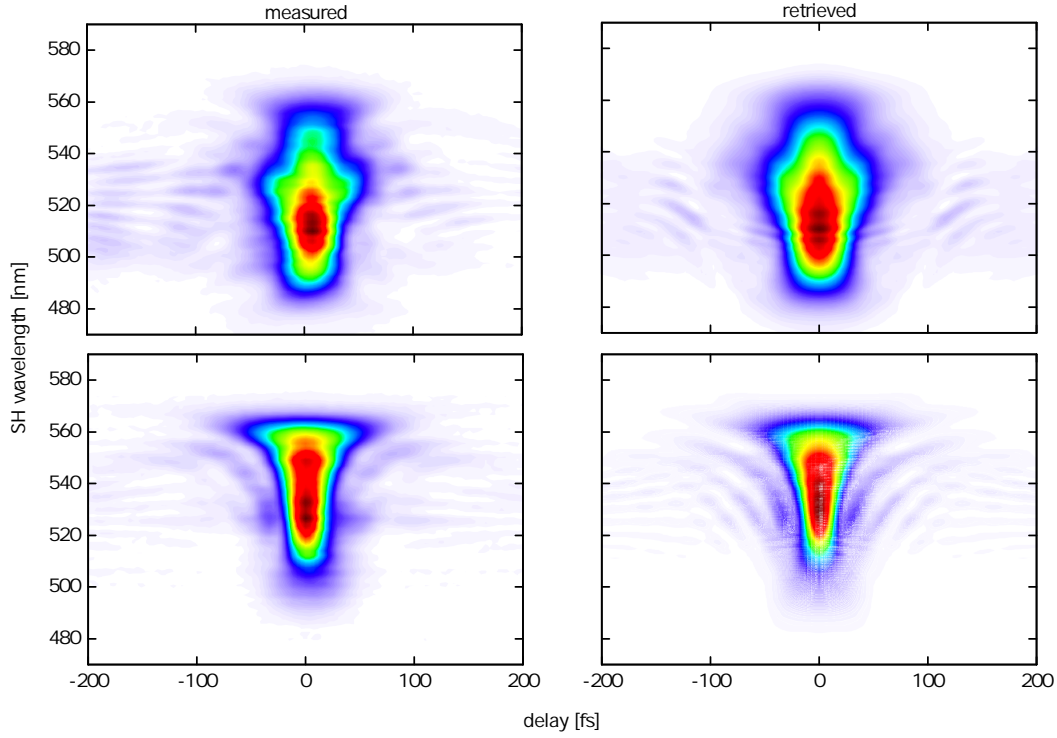


Figure 3.12: Input (top) and intracavity (bottom) FROG trace for the measurement with 24 mbar of air in the cavity. The respective FROG errors are $G = 0.013$ and $G = 0.005$ for a grid size of 512×512 pixels.

optimized and an intracavity pulse duration around 25 fs was measured. In both cases, the two methods show good agreement, indicating an accurate characterization of the intracavity pulse. The optimal offset frequency of the cavity was half the repetition rate which makes this cavity suitable for field sensitive experiments like HHG in a cavity [21].

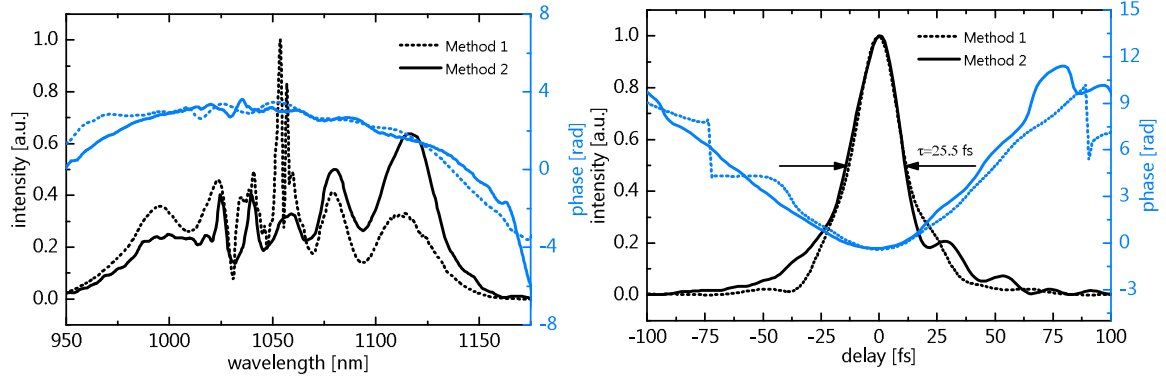


Figure 3.13: Intracavity spectrum (left) and field (right) (and respective phases) with 24 mbar of ambient air in the cavity. Dotted lines represent measurements with Method 1, solid lines with Method 2.

3.2 Intracavity spectral broadening and pulse compression

In section 3.1, the pulses that are sent to the cavity, are spectrally broadened in a fibre and compressed with CMs before being enhanced in the cavity. As a proof-of-principle for a possible alternative way of pulse compression, we directly sent the 160 fs-pulses from the Yb-based fibre amplifier to the cavity and placed a 100- μm -thick FS substrate in the cavity focus for spectral broadening via SPM [49]. We measured spectral bandwidths of 240 nm at -30 dB, that could support 20-fs pulses. An IC with shaped reflectivity was used to raise the level of the broadened parts of the spectrum. Furthermore, these results initiated the theoretical investigations of the applicability of the nonlinear cavity for spectroscopy, discussed in section 4.

3.2.1 Setup

The modified setup for the intracavity spectral broadening can be seen in figure 3.14. We bypassed the fibre broadening and CM compression from the setup in section 3.1 and directly coupled the 160 fs-pulse from the fibre amplifier to the cavity. The modematching (see section 2.2) was adjusted with two lenses in the beam path before

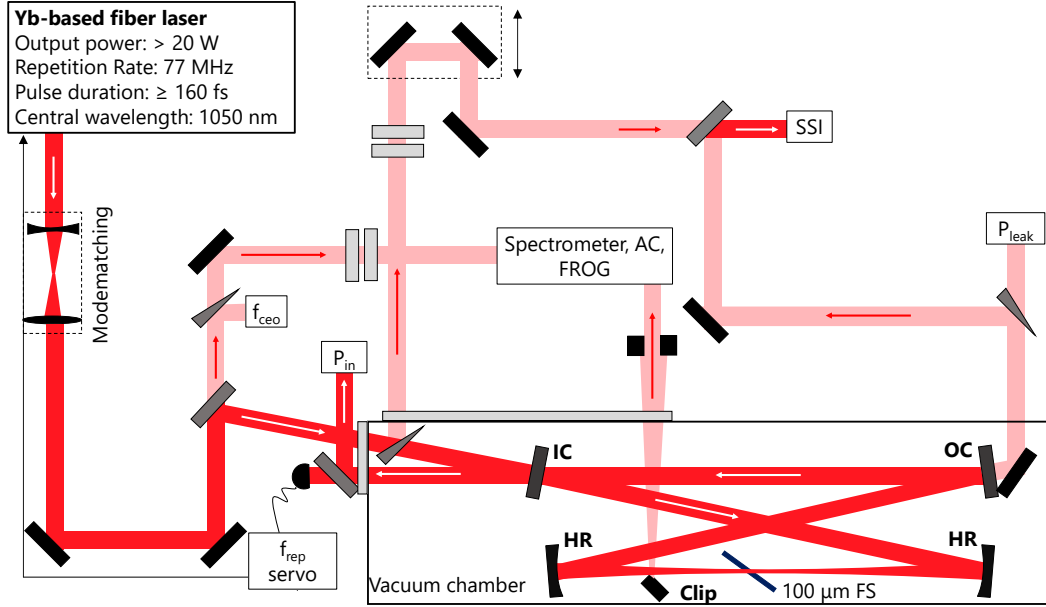


Figure 3.14: Setup for the intracavity spectral broadening experiment. In contrast to the ultrabroadband cavity setup, the fibre broadening and CM compression is removed. Two lenses are added to the setup for adjusting the modematching. A $100\ \mu\text{m}$ thick FS substrate is placed in the focus in Brewster’s angle.

the cavity. We placed a $100\text{-}\mu\text{m}$ -thick FS substrate in the focus of the cavity in Brewster’s angle for intracavity spectral broadening via SPM. The cavity mirrors are the same as in section 3.1.

3.2.2 Results

Proof of principle

As a proof of principle, we varied the input power and measured the intracavity spectra with an optical spectrum analyser (OSA) and the intracavity power from the leakage P_{leak} . For each input power, we optimized the offset of the cavity lock and the f_{ceo} of the input pulse train to reach the maximally broadened spectrum. The first corresponds to a change of the repetition rate of the laser at the lock wavelength. This was necessary, as the intracavity nonlinearity slightly changes the effective cavity length. The left part of figure 3.15 shows the spectra we measured for different input powers, where

the black line is the input spectrum, centered around 1047 nm and about 7 nm broad. A clear increase in broadening with increasing input power can be seen. The level of the broadened parts of the spectrum is 20 – 25 dB below the maximum value. We reached a -30 dB bandwidth of 240 nm in the broadest case. The nonlinear phase of the SPM causes the clamping [21, 52, 53] of the intracavity power, depicted in the right part of that figure. In combination with the non-flat mirror phase (see section 3.1), this made further broadening impossible.

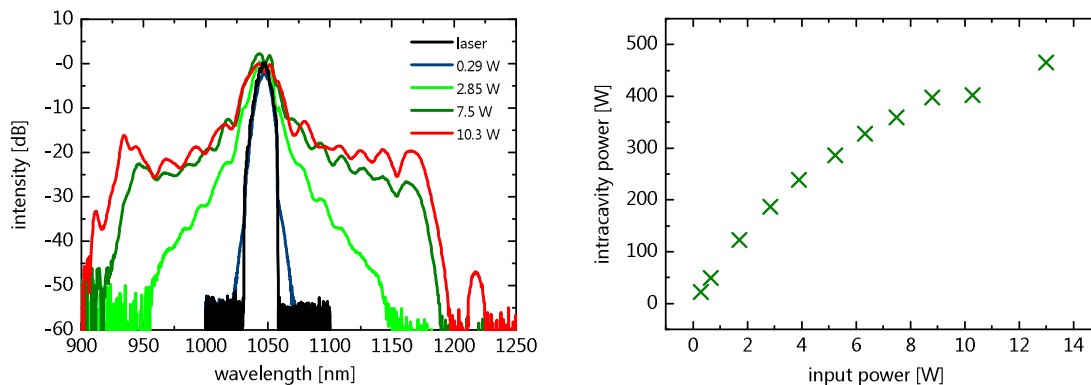


Figure 3.15: Left: Broadened intracavity spectra for different input powers. The black line shows the input spectrum. The broadest bandwidth at -30 dB is around 240 nm and the level of the broadened spectral components is 20 – 25 dB below the maximum. Right: Intracavity power as a function of input power. The clamping is caused by the nonlinear phase of the spectral broadening.

We calculated the intracavity pulse shapes for bandwidth limited pulses and their respective FT limits. These are shown in figure 3.16.

The minimum calculated FT limit is 20 fs, which is about the same as the shortest measured pulse duration in the ultrabroadband cavity. A further measure for the increasing nonlinearity is the wavelength- and input-power-dependent mode size, which is shown in figure 3.17. The larger the wavelength, the bigger the relative mode size (as described in section 2.2) and the higher the input power, the bigger the average mode size gets, because of the Kerr lensing effect [49].

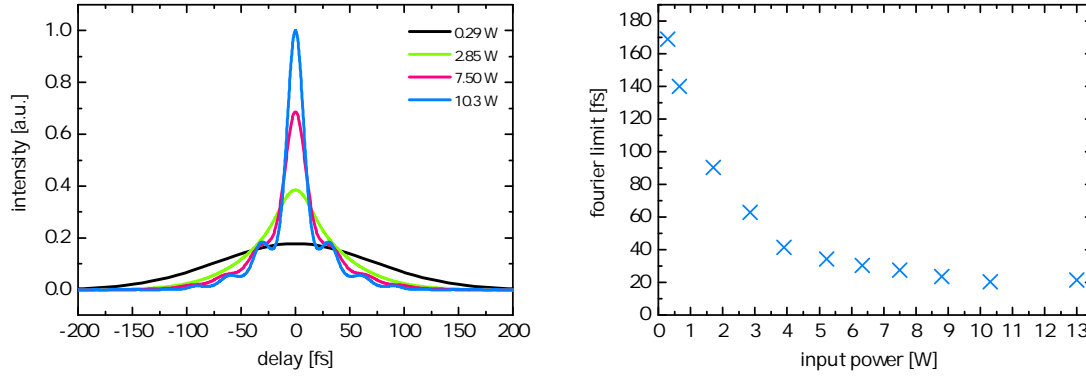


Figure 3.16: Left: Calculated intracavity fields for FT limited pulses. Right: Respective FT limits, with a minimum of 20 fs

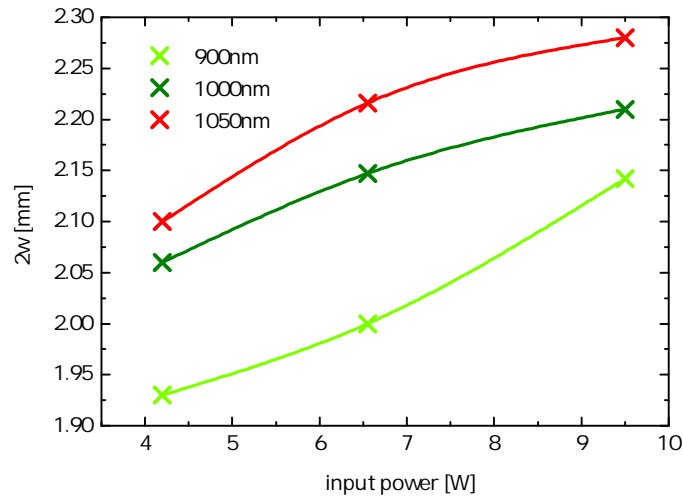


Figure 3.17: Intracavity mode-size as a function of input power for three different wavelengths. The size increases with wavelength and input power, being a measure for the increasing nonlinearity of the cavity.

Input coupler with shaped reflectivity

To lift the level of the broadened parts of the spectrum, we used an IC with a transmission curve shaped as depicted in the left part of figure 3.18.

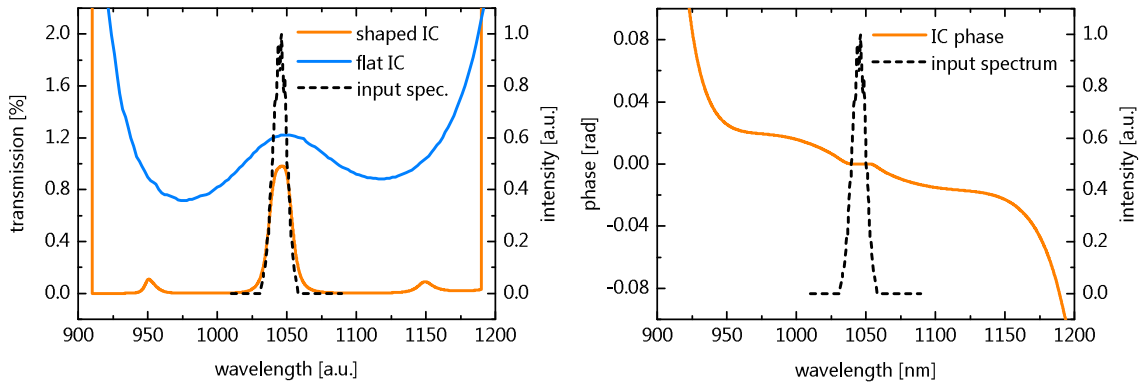


Figure 3.18: Left: Designed transmission curve of the IC, aimed to lift the level of the broadened parts of the spectrum. Dotted line: Input spectrum. The transmission curve of the IC used before is shown for comparison. Right: Designed phase of the IC. Dotted line: input spectrum.

For comparison, this figure also shows the transmission curve of the IC that we used before. Additionally, the phase caused by the transmission is shown in the right part of that figure. The transmission of the IC is around 1% at the position of the input spectrum and almost zero at the outer parts. In addition to the reshape of this transmission curve, we replaced the second IC with a HR mirror, resulting in an IC limited cavity. The broadest spectra we measured with this configuration can be seen in figure 3.19.

The broadened parts of the spectrum were raised up to 10 – 15 dB below the peak, spanning again about 240 nm at -30 dB. For the measurement of the intracavity pulse duration and phase, we acquired FROG traces. We changed the cavity dispersion by varying the chamber pressures, to check whether we could easily compensate for the nonlinear phase, which would result in shorter pulse durations. The resulting traces can be seen in figure 3.20 with a logarithmic intensity scale.

From top to bottom, the settings were: 1) input pulse. 2) intracavity pulse for 15.5 W input power, 10^{-2} mbar of air. 3) same parameters, different f_{ceo} . 4) same input power,

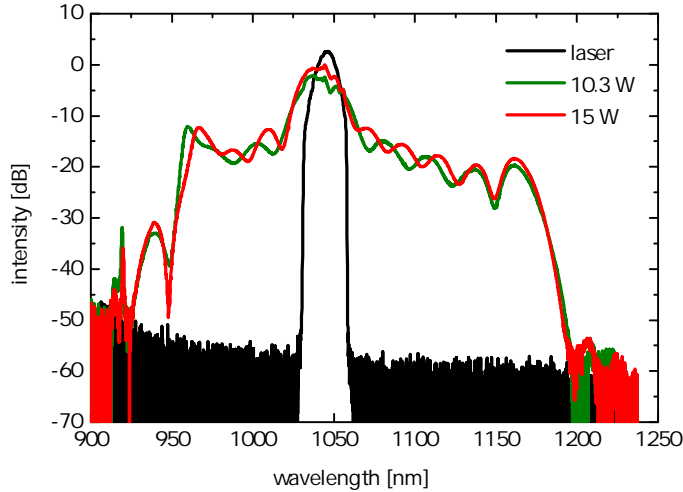


Figure 3.19: Broadened spectra, reached with an IC with shaped transmission and by replacing the second cavity IC with a HR mirror. The bandwidth at -30 dB is around 240 nm, the level of the broadened parts of the spectrum is now 15 – 20 dB below the maximum value.

44 mbar. 5) 16 W input power, same pressure. 6) same input power, 110 mbar.

No clear dependence on the cavity pressure can be seen. This can be caused by the strongly drifting CE offset frequency (f_{ceo}) of the laser which seemed to greatly affect the broadening among other uncertainties like the cavity lock offset. The necessary dispersion needed for the pulse compression could be calculated from a measurement or simulation of the cavity roundtrip phase in steady state. The retrieved spectrum (left) and field (right) for the lowest IC pressure (FROG error $G = 0.002$ for a grid size of 512×512 pixels) is shown in figure 3.21.

The measured and retrieved spectra agree quite well, even for the very weak spectral components. The pulse is not automatically shortened by the nonlinear process, but also not lengthened in time, showing that the dispersion of the FS substrate does not drastically influence the pulse shape. The retrieved phase suggests that it could be compensated for by adjusting the cavity dispersion or shape the mirror phase accordingly. This is not trivial, because the nonlinearity increases with shorter pulse durations. Therefore, a steady state, supporting self compression, that can be reached

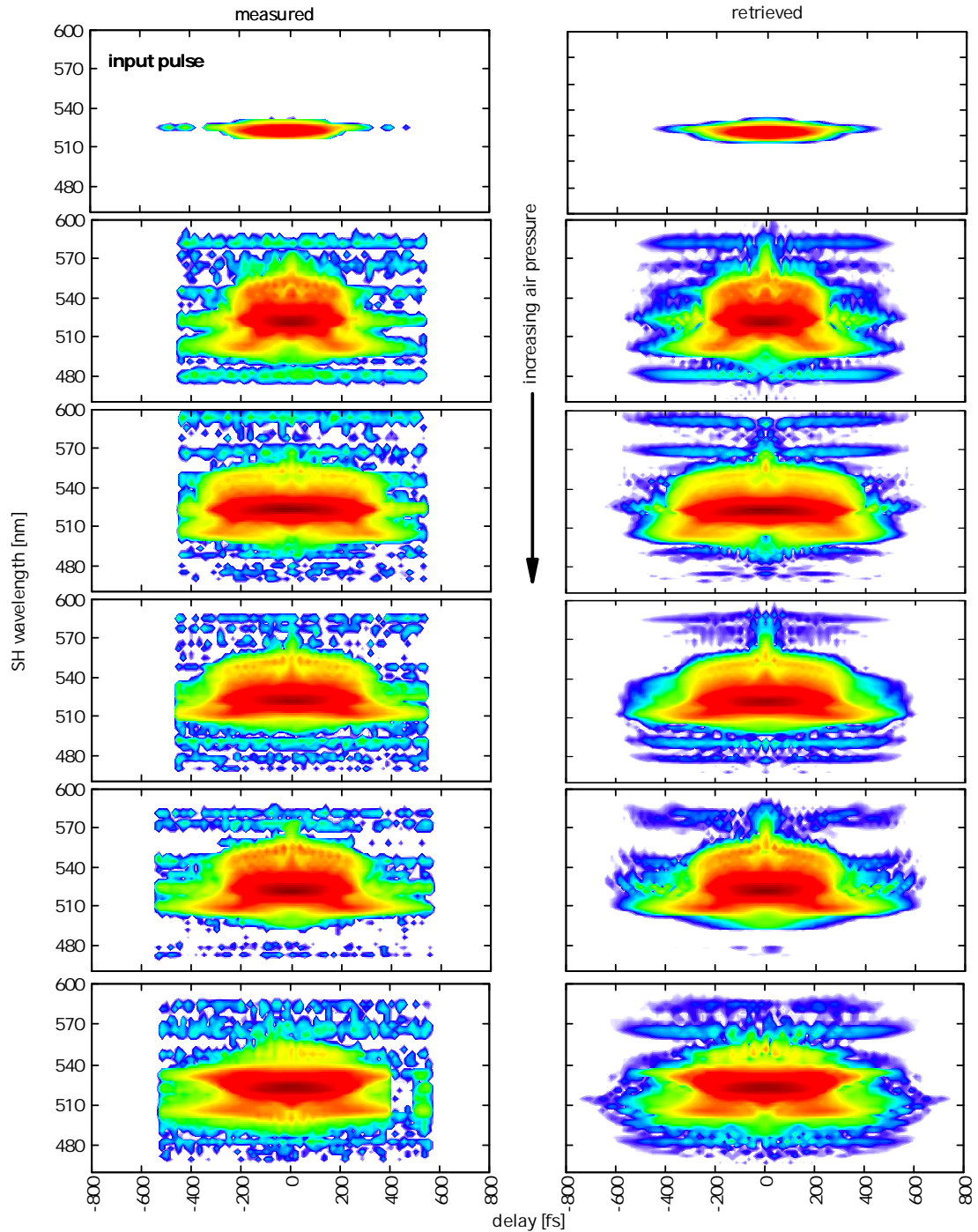


Figure 3.20: Frog traces for different vacuum chamber pressures (logarithmic scale). From top to bottom, the settings were: 1) input pulse. 2) intracavity pulse for 15.5 W input power, 10^{-2} mbar of air. 3) same parameters, different f_{ceo} . 4) same input power, 44 mbar. 5) 16 W input power, same pressure. 6) same input power, 110 mbar.

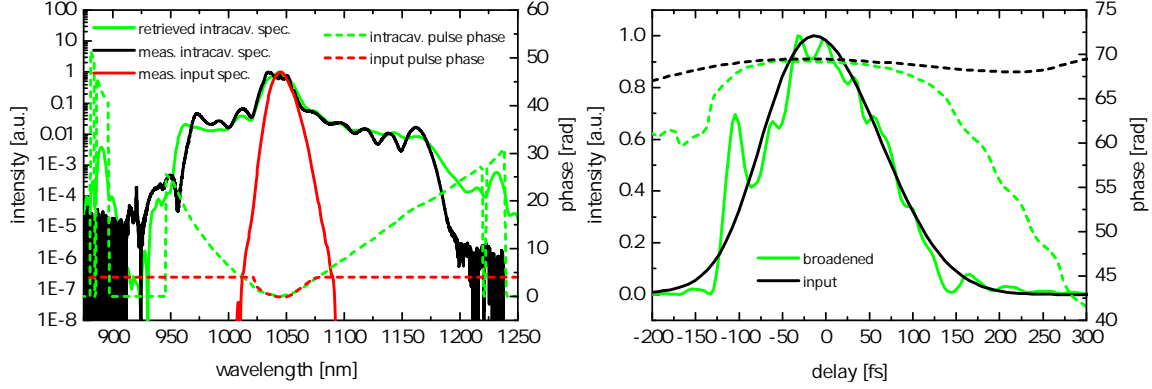


Figure 3.21: Left: Retrieved spectrum and spectral phase, as well as intracavity spectrum measured with the OSA. For comparison, the red lines show the input spectrum and phase. Even for the spectral components with low intensity, the agreement is quite good. Right: retrieved intensity envelope and phase in the time domain. The black curves show the input pulse and phase. The FROG error was $G = 0.002$ for a grid size of 512×512 pixels.

with a fixed phase, has to be found. Finding such a steady state requires further theoretical and experimental investigations. For meaningful experiments f_{ceo} stabilization would be necessary. The goal is to compensate the nonlinear phase of the broadening with the cavity mirrors and compress the pulses in the cavity. Further experiments regarding this goal will be done with a CE phase stabilized laser system like the one described in [54]. If the compression works out fine, this cavity would be an alternative source for the generation of isolated attosecond pulses [14]. Furthermore, the question arises, whether such a cavity would be suited for intracavity spectroscopy despite the nonlinearity. We addressed this question with simulations in the following chapter.

Chapter 4

Simulation of intracavity spectral broadening

In the following, the question, whether the pulses, broadened in the cavity, as described in section 3.2, are suited for cavity enhanced spectroscopy, is investigated. More precisely, the question whether the effective interaction length of the resonator is reduced too much by the nonlinearity, is addressed. As the bandwidth of the intracavity broadened pulses is the same as for the fibre-broadened pulses in chapter 3.1, this would be a possible alternative scheme to reach a bandwidth exceeding 200 nm, which would also be of tremendous interest for Raman spectroscopy or for vibrational IR spectroscopy, if applied in the molecular fingerprint region [16].

To this end, the interaction of spectral broadening via the Kerr nonlinearity with a linear absorption line in an EC was simulated with a 1D model. For describing the nonlinear spectral broadening, the first order propagation equation, neglecting dispersion is used [55] and the linear absorption is described with the Lorentz Model [56,57]. As a reference, the simulated interaction lengths are compared to the ones in a linear cavity, where the single-pass interaction length is enhanced by $Finesse/\pi$ [17].

This chapter starts with a description of the first order propagation equation as a model for the propagation of laser pulses through a nonlinear Kerr medium. Furthermore, the simulation of the buildup of a steady state in a nonlinear EC is shown. Finally, the influence of the Kerr nonlinearity on the path length enhancement (PLE) of an EC is investigated and the resulting applicability for spectroscopy is discussed.

4.1 Propagation of laser pulses through a Kerr medium

For the description of the propagation of a laser pulse through a nonlinear medium, one starts from the scalar wave equation in the frequency domain, which is derived from Maxwell's equations [49, 58] and given by the following formula [55]:

$$[\partial_z^2 + \nabla_{\perp}^2 + k^2(\omega)] E(\mathbf{r}, \omega) = \frac{\omega^2}{\epsilon_0 c^2} \mathcal{F}_t [P_{\text{nl}}(\mathbf{r}, t)] \quad (4.1)$$

Here, \mathcal{F}_t is the FT and P_{nl} the nonlinear polarization of the medium. Equation 4.1 can be simplified with the ansatz $E(\mathbf{r}, \omega) = U(\mathbf{r}, \omega)e^{ik(\omega)z}$, where U is the spatially varying complex envelope of the electric field in the frequency domain [58]. With the assumption of the slowly evolving envelope [55] and neglecting transverse spatial dependences for a 1D model, we obtain:

$$\frac{\partial U(z, \omega)}{\partial z} = \frac{i\omega^2 \mu_0}{2k(\omega)} e^{-ik(\omega)z} \cdot \mathcal{F}_t [P_{\text{nl}}(\omega)] \quad (4.2)$$

The term $e^{-ik(\omega)z}$ accounts for linear dispersion, which will be neglected in the following. Therefore, the refractive index $n(\omega)$ will also be set to 1 for all wavelengths.

This differential equation can be solved with a finite difference method as in equation 4.3 [58].

$$U(z + \Delta z, \omega) \approx U(z, \omega) + \Delta z \cdot \frac{\partial U}{\partial z} \quad (4.3)$$

Here, $\frac{\partial U}{\partial z}$ is given by equation 4.2 and the stepsize Δz has to be chosen small enough, that the calculations do not change with further decrease.

For the Kerr effect, the nonlinear polarization P_{nl} is given in the time domain by [49]:

$$P_{\text{nl}}(t) = \epsilon_0^2 n_2 n_{\text{R}}^2 c |A_{\text{k}}(t)|^2 A_{\text{k}}(t), \quad (4.4)$$

where n_2 is the material specific nonlinear refractive index, which indicates the strength of the nonlinearity. For FS it is $3.2 \cdot 10^{-16} \text{ cm}^2/\text{W}$ [59]. As everything is calculated in a 1D model, the electric field is normalized to the peak intensity in the focus ($A_{\text{norm}}(t)$), because the substrate will be placed there. The normalization factor can be calculated

from the input power P_{in} , the laser repetition rate f_{rep} and the focus size A_{focus} as follows [60]:

$$\frac{|A_{\text{norm}}(t)|}{|A(t)|} = \sqrt{\frac{2P_{\text{in}}}{f_{\text{rep}}A_{\text{focus}} \int A(t)dt}} \quad (4.5)$$

In the following, every input field is normalized that way and the index 'norm' is neglected. With the given nonlinear polarization and the propagation equation, the propagation through the FS substrate can be calculated with equation 4.6.

$$A_{k,\text{nl}}(\omega) = A_k + \frac{i\Delta z\omega}{2c\epsilon_0} \mathcal{F}_t [P_{\text{nl}}(t)] \quad (4.6)$$

4.2 Buildup in a nonlinear enhancement cavity

In the frequency domain, the build-up of the intracavity pulse is given by equation 4.7 [20].

$$A_{k+1}(\omega) = \sqrt{T_{\text{ic}}(\omega)}A_{\text{in}}(\omega) + \sqrt{R_{\text{ic}}(\omega)}\sqrt{A(\omega)}e^{i\varphi_{\text{cav}}(\omega)}A_k(\omega) \quad (4.7)$$

Here, T_{ic} and R_{ic} are the frequency dependent amplitude transmission and reflectivity of the cavity IC, respectively. The overall cavity losses are denoted as A and φ is the cavity phase. The complex envelope of the incoming pulse is given by A_{in} and the circulating one of the previous round-trip by A_k .

Together with the nonlinear propagation from the previous section and starting with an empty cavity, the nonlinear buildup of the intracavity pulse is calculated as follows:

1. Field in the frequency domain after the IC: $A_1(\omega) = A_{\text{in}}(\omega)\sqrt{T_{\text{ic}}(\omega)}$
2. FT to the time domain for the calculation of the nonlinearity: $A_1(t) = \mathcal{F}_t(A_1(\omega))$
3. Calculate $P_{\text{nl},1}(t)$ from equation 4.4
4. Calculate the field in the frequency domain after the nonlinearity $A_{k,\text{nl}}(\omega)$ from equation 4.6.
5. Propagate through the cavity according to equation 4.7 to calculate A_k .

6. Repeat everything from point 2 (with A_k instead of A_1), until a steady state is reached.

4.3 Kerr nonlinearity vs. linear absorption in a cavity

The linear absorption can, for example be described with the Lorentz Oscillator Model [56,57] in the frequency domain, which will be explained shortly in the following. The susceptibility is a complex number:

$$\frac{\tilde{\epsilon}}{\epsilon_0} = \epsilon_r - i\epsilon_i, \quad (4.8)$$

where the real (ϵ_r) and imaginary (ϵ_i) part is given by:

$$\epsilon_r = 1 + \frac{\omega_p^2 (\omega_0^2 - \omega^2)}{(\omega_0^2 - \omega^2)^2 + \omega^2 \gamma^2} \quad (4.9)$$

and

$$\epsilon_i = \frac{\omega_p^2 \omega \gamma}{(\omega_0^2 - \omega^2)^2 + \omega^2 \gamma^2}, \quad (4.10)$$

respectively. The center of the absorption line is at ω_0 and γ is a measure for the decay time, corresponding to the width of the line. The plasma frequency ω_p is a measure for the depth of the line. As the susceptibility is complex, the same holds true for the refractive index $n(\omega) = \sqrt{\epsilon(\omega)}$:

$$n(\omega) = n_r(\omega) - in_i(\omega) \quad (4.11)$$

The imaginary part is often renamed $n_i(\omega) = \kappa(\omega)$, where κ is called the extinction coefficient, which accounts for the absorption, whereas the real part of the refractive index describes dispersion.

The real (n_R) and imaginary (κ) parts of the refractive index can be calculated from ϵ_r and ϵ_i in the following way:

$$n_{\text{R}} = \frac{1}{\sqrt{2}} \sqrt{\epsilon_{\text{r}} + \sqrt{\epsilon_{\text{r}}^2 + \epsilon_{\text{i}}^2}} \quad (4.12)$$

$$\kappa = \frac{1}{\sqrt{2}} \sqrt{-\epsilon_{\text{r}} + \sqrt{\epsilon_{\text{r}}^2 + \epsilon_{\text{i}}^2}} \quad (4.13)$$

With this complex refractive index, the frequency dependent transmittance $t_{\text{abs}}(\omega)$ is given by:

$$t_{\text{abs}}(\omega) = \frac{1}{\cos(\varphi(\omega)) + \frac{i}{2} \left(n_{\text{R}}(\omega) + \frac{1}{n_{\text{R}}(\omega)} \right) \sin(\varphi_{\text{d}}(\omega))} \quad (4.14)$$

Here, $\varphi_{\text{d}}(\omega)$ is the so-called phase thickness of a material layer with real thickness d :

$$\varphi_{\text{d}}(\omega) = \frac{2\pi}{\omega} n_{\text{R}}(\omega) d. \quad (4.15)$$

For the simulation of linear absorption in an EC, the GD caused by the absorption has to be taken into account. As this can be compensated with the cavity lock, a linear fit can be subtracted from the phase of t_{abs} .

The absorption is implemented in the cavity build-up with a multiplication in the frequency domain:

$$A_{\text{abs},k+1}(\omega) = \sqrt{T_{\text{ic}}(\omega)} A_{\text{in}}(\omega) + \sqrt{R_{\text{ic}}(\omega)} \sqrt{A(\omega)} e^{i\varphi_{\text{cav}}(\omega)} A_{\text{k}}(\omega) t_{\text{abs}}(\omega) \quad (4.16)$$

Validation of the linear absorption model

For the validation of the linear absorption model, the PLE calculated with the cavity build-up was compared to the theoretical value for a ring resonator. The relative dip depth after linear absorption in a single pass through a cavity of length L is calculated with Beer's law:

$$\frac{I_{\text{dip,single}}(\omega_0)}{I_0} = e^{-\alpha L} \quad (4.17)$$

where the attenuation coefficient α can be calculated from the extinction coefficient κ

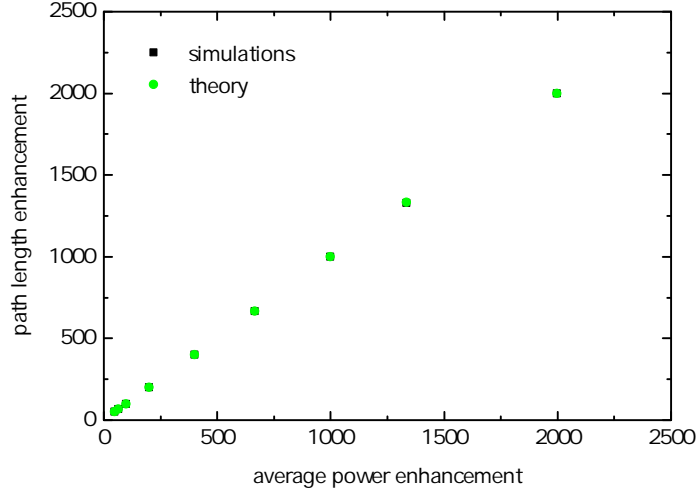


Figure 4.1: Validation of the linear absorption model in an impedance matched EC. The simulated PLE as a function of average power enhancement is the same as the theoretical value of \mathcal{F}/π for all data points.

via $\alpha = 4\pi\kappa/\lambda_0$ for the wavelength λ_0 [61]. For an EC in the steady state with finesse \mathcal{F} , this equation changes to:

$$\frac{I_{\text{dip,cav}}(\omega_0)}{I_{0,\text{cav}}} = (e^{-\alpha L})^{\mathcal{F}/\pi} \quad (4.18)$$

[17]. Here, $I_{\text{dip,single}}$ and $I_{\text{dip,cav}}$ are the intensities at the dip position in the steady state with absorption, and $I_{0,\text{single}}$ and $I_{0,\text{cav}}$ the respective values without absorption. The results of the validation for different average power enhancements can be seen in figure 4.1, for a single pass absorption of about 0.3 ppm. The y-axis shows the effective PLE, which is the effective interaction length, normalized to the single pass value. It is given by:

$$PLE = \frac{\ln(I_{\text{dip,cav}}/I_{0,\text{cav}})}{\ln(I_{\text{dip,single}}/I_{0,\text{single}})} \quad (4.19)$$

and equals \mathcal{F}/π for a linear cavity.

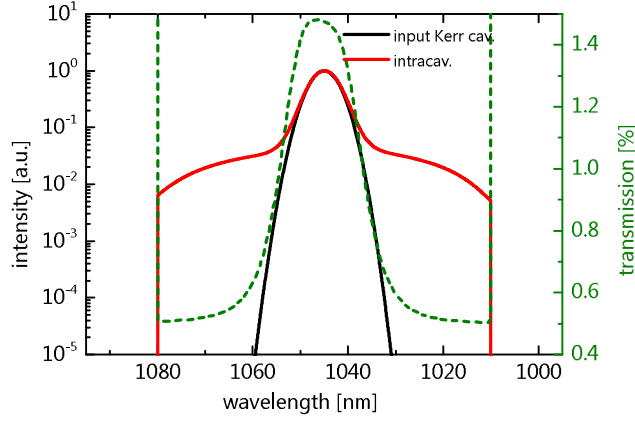


Figure 4.2: Input and intracavity spectrum for the simulation of the nonlinear cavity buildup. The dotted line shows the transmission of the IC.

Nonlinear cavity

The goal of these simulations was the investigation of a possible change in PLE compared to the linear case, when there is nonlinear broadening in a FS substrate inside the cavity. Therefore, the effective PLE for different absorption dip positions, nonlinearity strengths (varied via the thickness of the FS substrate) and cavity average power enhancements (varied via the IC transmission) was compared for two cases:

1. Calculate the nonlinear cavity buildup for a Gaussian input spectrum with 7 nm bandwidth (FWHM). The transmission of the IC is set to 1 below 1010 nm and above 1080 nm. It is shaped dip-like in the spectral region of the input spectrum, with a peak of about 1.5% and decreasing to 0.5% outside the input spectral range. Both, the input spectrum and IC transmission are depicted in figure 4.2, together with the broadened intracavity spectrum in the steady state.

The simulations are made for an impedance matched cavity, meaning that the cavity losses are equal to the IC transmission. The spectral phase of the mirrors is assumed to be flat over the whole considered bandwidth and is set to zero after each roundtrip. This assumption leads to a pulse shortening because of the spectral broadening. For the experimental implementation, extended simulations and designs of mirror phase shapes would be necessary. The compensation during

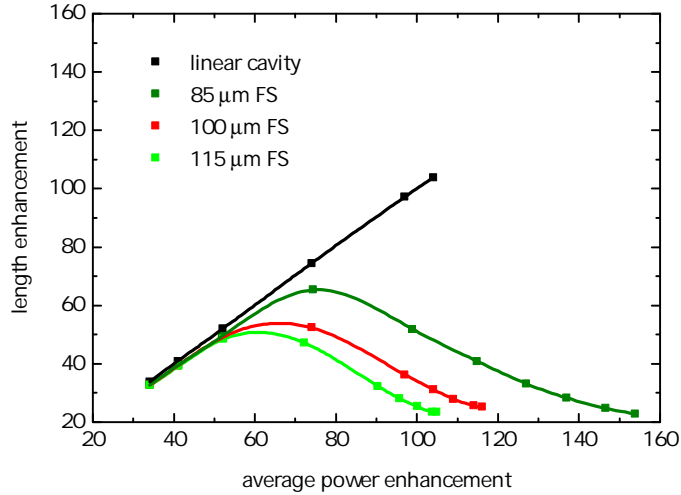


Figure 4.3: PLE for different average power enhancements and plate thicknesses with an absorption dip at the center of the input spectrum. For comparison, the black line shows the PLE of the linear cavity.

the buildup would not be possible because of the change of the nonlinearity with the pulse duration. After reaching a steady state, the average power enhancement U is calculated as the ratio of the intracavity power to the input power. In this steady state, several roundtrips including absorption are calculated, until a steady state is reached again.

2. A uniform IC transmission $t_{IC} = 1/U$ is calculated, that leads to the same average power enhancement as in (1) [20]. Then, the broadened spectrum from the nonlinear buildup is taken as the input to the simulation of a linear buildup. Again, the linear absorption is added in steady state and several roundtrips are calculated until a new steady state is reached.

Figure 4.3 shows the path length enhancement for different average power enhancement values and plate thicknesses. The absorption line is located at the center of the input spectrum and the single pass absorption is about 0.3 ppm. The PLE for the linear case is shown for comparison.

The PLE is below the linear value for all plate thicknesses. This can be caused by a combination of the shape of the input coupler transmission and the nonlinearity, which

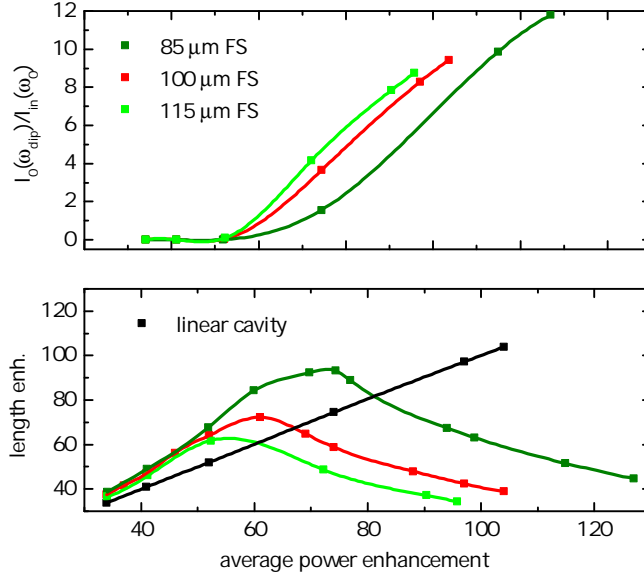


Figure 4.4: Upper panel: Intensity at the absorption wavelength (20 nm above the center of the input spectrum) in steady state without absorption as a measure of the potentially available signal and the nonlinearity for different plate thicknesses as a function of average power enhancement. Lower panel: PLE as a function of average power enhancement and for different plate thicknesses with an absorption dip 20 nm above the center of the input spectrum. The black line shows the linear case.

both decrease the finesse at this spectral component compared to the linear case.

Figure 4.4 shows the PLE for an absorption dip located at a central wavelength 20 nm longer than the central wavelength of the input spectrum and again a single pass absorption of ≈ 0.3 ppm. The upper part of that figure shows the relative intensity without absorption (compared to the peak value) as a measure for the nonlinearity and the potentially available signal at that wavelength.

In this case, the PLE differs strongly between high and low average power enhancements. For lower values, it surpasses the linear values, whereas it decreases strongly in the higher range. Furthermore, an increase of the PLE for thinner plates can be seen. This could be caused by the reduced blurring of the spectral components for thinner plates, which correspond to a lower effective nonlinearity. Furthermore, the transmission of the IC is almost zero in that wavelength range which leads to a very

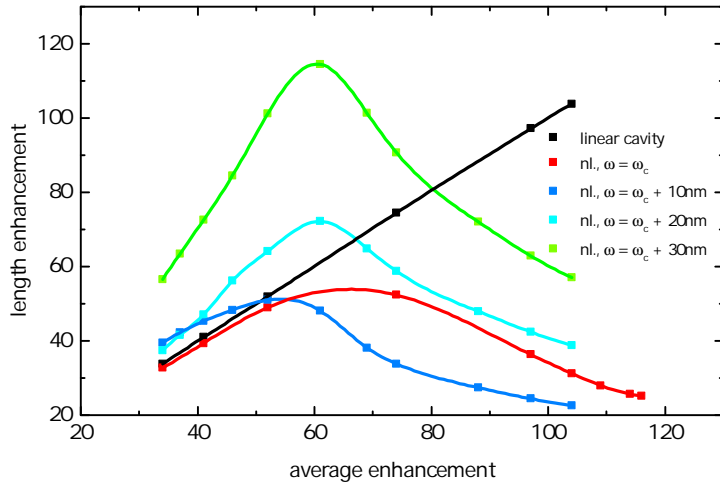


Figure 4.5: Path length enhancement for different average power enhancements and dip positions. The PLE is higher for absorption lines with increased distance from the center of the spectrum, most likely due to the decreased nonlinearity and IC transmission. The black line again shows the linear case.

high finesse. Nevertheless, the overall available signal is reduced compared to the higher nonlinearities. Therefore, a tradeoff of available signal and sensitivity might have to be made.

The dependence of the PLE on the dip position with respect to the center of the spectrum can be seen in figure 4.5.

It increases for larger distances from the center, most likely because the nonlinearity is reduced, the further the wavelength is away from the central region and the IC transmission decreases.

In conclusion, the combination of the Kerr nonlinearity and the linear absorption seems promising, because the PLE can surpass the linear value for certain configurations. Furthermore, it would make broadband spectroscopy possible without an external broadening mechanism. Further investigations into the applicability for spectroscopy are necessary, addressing even lower nonlinearities and higher average power enhancements. Furthermore, the second shaped IC (impedance matched cavity) should be

replaced by a HR mirror or by one with a uniform transmission for the same output coupling efficiency for all wavelengths. The detection of the absorption also has to be taken into account to have a measure for the influence of the nonlinearity on the sensitivity enhancement of the cavity for spectroscopy.

Nevertheless, the results show, that absorption spectroscopy should still be possible with the nonlinearity and provide a further motivation for the intracavity pulse compression of the broadened spectra from section 3.2.

Chapter 5

Conclusion and outlook

In conclusion, we demonstrated an unprecedented intracavity pulse duration of sub 20 fs in a high finesse enhancement cavity. This was only possible after a long design and coating process of the cavity mirrors. With mirrors that partially compensated for each others dispersion, a spectral bandwidth of > 150 nm at an enhancement of ≈ 70 and a finesse of ≈ 540 was shown. The bandwidth could be extended even more, by adding 24 mbar of air to the cavity for further dispersion compensation. The intracavity pulses were characterized with two different methods, consisting of a combination of FROG and SSI measurements. The resulting pulse durations of sub 20 fs for both methods are in very good agreement, which makes the pulse characterization very reliable. Regarding applications, this cavity would be suitable for stimulated Raman spectroscopy, where its spectral bandwidth spans half the molecular fingerprint region [16]. The current intracavity spectrum could be used as the Stokes pulse, and a narrow pump pulse would have to be generated, for example from the blue part of the spectrum.

Furthermore, as the demonstrated pulse duration corresponds to 5.4 oscillation cycles of the electric field, we are already in the few-cycle regime. With a suitable gating method [14], isolated attosecond pulses could be generated via HHG [13]. Furthermore, the high repetition rate would make high resolution intracavity spectroscopy in the extreme ultraviolet feasible [28], because of the resulting widespread comb lines.

In the second experiment, we bypassed the external spectral broadening and pulse compression before the cavity and inserted a $100 - \mu\text{m}$ thick FS substrate in the cavity focus for spectral broadening via self-phase modulation. With an IC with shaped

transmission in an IC-limited cavity, we could produce spectra with a -30 -dB bandwidth of 240 nm, that would support 20 fs. The level of the broadened parts of the spectrum was $15 - 20$ dB below the peak value.

In principle, only an oscillator, that delivers the pulse train and an EC are necessary for intracavity experiments. However, for ultra-broadband spectra/ultra-short pulses, an additional spectral broadening and compression scheme is needed. The intracavity spectral broadening would make an external compression unnecessary and therefore reduce the system to as few components as possible, which would be advantageous because of its simplicity.

Nevertheless, for the intracavity pulse compression, mirrors would have to be designed, that compensate for the nonlinear phase caused by the broadening. This would be challenging, as the nonlinearity increases with decreasing pulse duration. Further experiments regarding the nonlinear cavity should be done in a CE -phase stabilized system like the one described in [54], in order to minimize the number of unknown parameters with influence on the spectral bandwidth. A possible application of the intracavity broadened pulse, for which the pulse compression would not be necessary, is cavity enhanced absorption spectroscopy [4, 5].

We theoretically investigated the applicability of the nonlinear cavity for this purpose, by simulating the influence of the broadening on the sensitivity of the cavity on a linear absorption line. For certain configurations, namely low average power enhancements and nonlinearities, the nonlinear PLE surpassed the linear value of \mathcal{F}/π . Further simulations, considering even lower nonlinearities and higher average power enhancements would be necessary to find out about advantages and disadvantages of the nonlinear cavity compared to a linear one. Furthermore, the measurement process of the absorption lines would have to be taken into account and a measure for the true change in sensitivity in an actual experiment should be found.

Chapter 6

Bibliography

- [1] R. J. Jones et al. *Femtosecond pulse amplification by coherent addition in a passive optical cavity*. Optics Letters, **27**(20), 1848 (2002).
- [2] C. Gohle et al. *A frequency comb in the extreme ultraviolet*. Nature, **436**(7048), 234–237 (2005).
- [3] R. J. Jones et al. *Phase-coherent frequency combs in the vacuum ultraviolet via high-harmonic generation inside a femtosecond enhancement cavity*. Physical review letters, **94**(19), 193201 (2005).
- [4] G. Gagliardi et al., eds. *Cavity-Enhanced Spectroscopy and Sensing*, vol. 179 of *Springer Series in Optical Sciences*. Springer Berlin Heidelberg, Berlin, Heidelberg and s.l. (2014).
- [5] T. Gherman et al. *Modelocked Cavity-Enhanced Absorption Spectroscopy*. Optics Express, **10**(19), 1033 (2002).
- [6] D. J. Taylor et al. *Enhanced Raman sensitivity using an actively stabilized external resonator*. Review of Scientific Instruments, **72**(4), 1970 (2001).
- [7] S.-i. Zaitsev et al. *Phase-matched Raman-resonant four-wave mixing in a dispersion-compensated high-finesse optical cavity*. Physical review letters, **100**(7), 073901 (2008).
- [8] A. Foltynowicz et al. *Cavity-enhanced optical frequency comb spectroscopy in the mid-infrared application to trace detection of hydrogen peroxide*. Applied Physics B, **110**(2), 163–175 (2013).

- [9] A. Cingoz et al. *Direct frequency comb spectroscopy in the extreme ultraviolet*. Nature, **482**(7383), 68–71 (2012).
- [10] F. Adler et al. *Cavity-enhanced direct frequency comb spectroscopy: technology and applications*. Annual review of analytical chemistry (Palo Alto, Calif.), **3**, 175–205 (2010).
- [11] B. Bernhardt et al. *Cavity-enhanced dual-comb spectroscopy*. Nature Photonics, **4**(1), 55–57 (2009).
- [12] S. Holzberger. *Enhancement cavities for attosecond physics*. Dissertation, LMU München, München (2015).
- [13] G. Sansone et al. *Isolated single-cycle attosecond pulses*. Science (New York, N.Y.), **314**(5798), 443–446 (2006).
- [14] M. Högnér et al. *Generation of Isolated Attosecond Pulses with Enhancement Cavities - a Theoretical Study* (in preparation, 2016).
- [15] A. P. Kovács et al. *Group-delay measurement on laser mirrors by spectrally resolved white-light interferometry*. Optics Letters, **20**(7), 788 (1995).
- [16] D. R. Dietze et al. *Femtosecond Stimulated Raman Spectroscopy*. ChemPhysChem, **17**(9), 1224–1251 (2016).
- [17] A. Foltynowicz et al. *Optical frequency comb spectroscopy*. Faraday discussions, **150**, 23–31; discussion 113–60 (2011).
- [18] J.-C. Diels et al. *Ultrashort laser pulse phenomena: Fundamentals, techniques, and applications on a femtosecond time scale*. Acad. Pr, Amsterdam u.a., 2. ed. ed. (2006).
- [19] T. Udem et al. *Optical frequency metrology*. Nature, **416**(6877), 233–237 (2002).
- [20] I. Pupeza. *Power Scaling of Enhancement Cavities for Nonlinear Optics*. Dissertation, LMU München, München (2011).
- [21] S. Holzberger et al. *Femtosecond Enhancement Cavities in the Nonlinear Regime*. Physical Review Letters, **115**(2) (2015).

-
- [22] Holzwarth et al. *Optical frequency synthesizer for precision spectroscopy*. Physical review letters, **85**(11), 2264–2267 (2000).
- [23] D. J. Jones. *Carrier-Envelope Phase Control of Femtosecond Mode-Locked Lasers and Direct Optical Frequency Synthesis*. Science, **288**(5466), 635–639 (2000).
- [24] W. Nagourney. *Quantum electronics for atomic physics and telecommunication*. Oxford graduate texts, Oxford Univ. Press, Oxford, 2. ed. ed. (2014).
- [25] S. Holzberger et al. *Enhancement cavities for zero-offset-frequency pulse trains*. Optics letters, **40**(10), 2165–2168 (2015).
- [26] D. Yost. *Development of an Extreme Ultraviolet Frequency Comb for Precision Spectroscopy*. Ph.D. thesis.
- [27] A. E. Siegman. *Lasers*. Univ. Science Books, Mill Valley, Calif. (1986).
- [28] A. Ozawa et al. *High harmonic frequency combs for high resolution spectroscopy*. Physical review letters, **100**(25), 253901 (2008).
- [29] J. Weitenberg et al. *Transverse mode tailoring in a quasi-imaging high-finesse femtosecond enhancement cavity*. Optics express, **19**(10), 9551–9561 (2011).
- [30] H. Carstens et al. *Large-mode enhancement cavities*. Optics express, **21**(9), 11606–11617 (2013).
- [31] R. Trebino. *Frequency-Resolved Optical Gating: The Measurement of Ultrashort Laser Pulses*. Springer, New York (2000).
- [32] R. Trebino et al. *Measuring ultrashort laser pulses in the time-frequency domain using frequency-resolved optical gating*. Review of Scientific Instruments, **68**(9), 3277 (1997).
- [33] J. Paye et al. *Measurement of the amplitude and phase of ultrashort light pulses from spectrally resolved autocorrelation*. Optics Letters, **18**(22), 1946 (1993).
- [34] K. W. DeLong et al. *Frequency-resolved optical gating with the use of second-harmonic generation*. Journal of the Optical Society of America B, **11**(11), 2206 (1994).

- [35] J. Itatani et al. *Attosecond streak camera*. Physical review letters, **88**(17), 173903 (2002).
- [36] Q. Wu et al. *Free-space electro-optic sampling of terahertz beams*. Applied Physics Letters, **67**(24), 3523 (1995).
- [37] I. Pupeza et al. *Highly sensitive dispersion measurement of a high-power passive optical resonator using spatial-spectral interferometry*. Optics express, **18**(25), 26184–26195 (2010).
- [38] K. W. DeLong et al. *Pulse retrieval in frequency-resolved optical gating based on the method of generalized projections*. Optics Letters, **19**(24), 2152 (1994).
- [39] K. W. DeLong et al. *Comparison of ultrashort-pulse frequency-resolved-optical-gating traces for three common beam geometries*. Journal of the Optical Society of America B, **11**(9), 1595 (1994).
- [40] K. W. DeLong et al. *Practical issues in ultrashort-laser-pulse measurement using frequency-resolved optical gating*. IEEE Journal of Quantum Electronics, **32**(7), 1253–1264 (1996).
- [41] S. Akturk et al. *Measuring spatial chirp in ultrashort pulses using single-shot Frequency-Resolved Optical Gating*. Optics Express, **11**(1), 68 (2003).
- [42] L. Lepetit et al. *Linear techniques of phase measurement by femtosecond spectral interferometry for applications in spectroscopy*. Journal of the Optical Society of America B, **12**(12), 2467 (1995).
- [43] C. Froehly et al. *Time impulse response and time frequency response of optical pupils.:Experimental confirmations and applications*. Nouvelle Revue d’Optique, **4**(4), 183.
- [44] P. Bowlan et al. *Measuring the spatiotemporal electric field of tightly focused ultrashort pulses with sub-micron spatial resolution*. Optics Express, **16**(18), 13663 (2008).
- [45] H. Carstens et al. *High-harmonic generation at 250 MHz with photon energies exceeding 100 eV*. Optica, **3**(4), 366 (2016).

-
- [46] N. Lilienfein et al. *High-finesse enhancement cavity for few-cycle pulses* (in preparation, 2016).
- [47] C. M. Heyl et al. *Noncollinear optical gating*. *New Journal of Physics*, **16**(5), 052001 (2014).
- [48] T. Eidam et al. *57 W, 27 fs pulses from a fiber laser system using nonlinear compression*. *Applied Physics B*, **92**(1), 9–12 (2008).
- [49] R. W. Boyd. *Nonlinear optics*. Elsevier/Academic Press, Amsterdam, 3. ed. ed. (2008).
- [50] R. Szipoecs et al. *Chirped multilayer coatings for broadband dispersion control in femtosecond lasers*. *Optics Letters*, **19**(3), 201 (1994).
- [51] R. W. P. Drever et al. *Laser phase and frequency stabilization using an optical resonator*. *Applied Physics B Photophysics and Laser Chemistry*, **31**(2), 97–105 (1983).
- [52] I. Pupeza et al. *Compact high-repetition-rate source of coherent 100 eV radiation*. *Nature Photonics*, **7**(8), 608–612 (2013).
- [53] D. C. Yost et al. *Power optimization of XUV frequency combs for spectroscopy applications Invited*. *Optics express*, **19**(23), 23483–23493 (2011).
- [54] T. Saule et al. *Phase-stable, multi- μ J femtosecond pulses from a repetition-rate tuneable Ti:Sa-oscillator-seeded Yb-fiber amplifier*. *Applied Physics B* (submitted, 2016).
- [55] T. Brabec et al. *Intense few-cycle laser fields: Frontiers of nonlinear optics*. *Reviews of Modern Physics*, **72**(2), 545–591 (2000).
- [56] R. Gross et al. *Festkörperphysik. Aufgaben und Lösungen*. DE GRUYTER, München (2014).
- [57] S. A. Furman et al. *Basics of optics of multilayer systems*. Series "Basics of", Ed. Frontières, Gif-sur-Yvette (1992).

- [58] M. Hoegner. *Optical High-Order Harmonic Generation in Gas Targets with Spatially Tailored Driving Fields*. Masters thesis, LMU München, München (2013).
- [59] K. H. J. Buschow, ed. *Encyclopedia of materials: Science and technology*. Elsevier, Amsterdam and New York (2001).
- [60] W. P. Putnam et al. *Bessel-Gauss beam enhancement cavities for high-intensity applications*. *Optics express*, **20**(22), 24429–24443 (2012).
- [61] E. Hecht. *Optics*. Addison-Wesley, Reading, Mass., 4. ed., internat. ed. ed. (2002).

List of Acronyms

AC = AutoCorrelation
AOM = Acousto-Optic-Modulator
BBO = Beta Barium Borate
CE = Carrier-Envelope
CM = Chirped Mirror
EC = Enhancement Cavity
FROG = Frequency Resolved Optical Gating
FS = Fused Silica
FSR = Free Spectral Range
FT = Fourier Transform
FWHM = Full Width at Half Maximum
GD = Group Delay
GDD = Group Delay Dispersion
HHG = High Harmonic Generation
HR = Highly Reflective
IC = Input Coupler
IR = InfraRed
LMA = Large Mode Area
NIR = NirInfraRed
OOF = Optimal Offset Frequency
OSA = Optical Spectrum Analyzer
PLE = Path Length Enhancement
PSD = Power Spectral Density
SH = Second Harmonic
SHG = Second Harmonic Generation
SPM = Self-Phase-Modulation
SSI = Spatial Spectral Interferometry
UV = UltraViolet

Eidesstattliche Erklärung

Ich erkläre hiermit an Eides statt und durch meine eigenhändige Unterschrift, dass ich die vorliegende Arbeit selbständig verfasst und keine anderen als die angegebenen Quellen und Hilfsmittel verwendet habe. Alle Stellen, die wörtlich oder inhaltlich den angegebenen Quellen entnommen wurden, sind als solche kenntlich gemacht.

München, am 04.10.2016